energies

MDPI

Article

Experimental Comparison of Sensible and Latent Heat Storage in a Packed-Bed Thermal Energy Storage System

Tomasz Spietz *, Szymon Dobras, Kinga Kulik, Rafał Fryza and Agata Czardybon

Institute of Energy and Fuel Processing Technology, Zamkowa 1, 41-803 Zabrze, Poland; sdobras@itpe.pl (S.D.); kkulik@itpe.pl (K.K.); rfryza@itpe.pl (R.F.); aczardybon@itpe.pl (A.C.)

* Correspondence: tspietz@itpe.pl

Abstract

Thermal energy storage (TES) is essential for improving the flexibility and efficiency of renewable and industrial energy systems. This study experimentally compares sensible and latent heat storage using basalt aggregate and an encapsulated phase change material (PCM), specifically 60 wt.% $NaNO_3$–40 wt.% KNO_3, as packed-bed materials under elevated-temperature operating conditions. Tests were conducted in an air-based TES rig at air flow rates of 60–120 kg/h, with packed bed temperatures exceeding 400 °C. Key parameters included temperature profiles, thermal power, energy storage, and recovery during charging and discharging phases. The results indicate that increasing the air flow rate accelerated thermal front propagation and improved charging and discharging power, but did not proportionally increase stored or recovered energy. The basalt bed achieved recovered volumetric energy densities of 108–160 MJ/m^3 at about 150 °C and 351–405 MJ/m^3 above 320 °C. The encapsulated solar salt bed reached higher values, from 412–508 MJ/m^3 near 290 °C to 523–626 MJ/m^3 at higher temperatures. Both materials showed high TES efficiencies, in the range of 80–94%. Encapsulated PCM significantly increased energy storage density in packed-bed TES systems, while basalt aggregate provides higher short-term thermal power output.

Keywords: basalt aggregate; binary nitrate salt; eutectic PCM; inorganic PCM; macroencapsulated PCM; packed-bed TES; solar salt

1. Introduction

The increasing demand for energy, together with the growing share of variable renewable energy sources and the need to recover industrial waste heat, has intensified interest in technologies that can improve the flexibility and efficiency of energy systems. Thermal energy storage (TES) is one of the key solutions enabling the temporal decoupling of heat supply and demand. By storing heat during periods of excess energy availability and releasing it when required, TES systems can support the integration of renewable energy, improve the utilization of industrial heat streams, and reduce primary energy consumption in heat-driven processes [1].

Thermal energy can be stored through sensible heat storage (SHS), latent heat storage (LHS), or thermochemical storage [2,3]. Sensible and latent heat storage are the most developed for medium- and high-temperature applications because of their technical maturity and scalability [4,5]. SHS stores energy by raising the temperature of a solid or liquid without a phase change. The stored energy depends on the material's mass, specific heat capacity, and the temperature difference between charging and discharging. LHS uses phase

Check for updates

Academic Editor: Andrea De Pascale

Received: 16 June 2026
Revised: 27 June 2026
Accepted: 2 July 2026
Published: 6 July 2026

Copyright: © 2026 by the authors. Licensee MDPI, Basel, Switzerland. This article is an open access article distributed under the terms and conditions of the Creative Commons Attribution (CC BY) license.

change materials (PCMs) that absorb or release heat during phase transitions, typically solid–liquid changes such as melting and solidification. This approach offers higher storage density within a narrower temperature range but presents design challenges related to heat transfer, volume change, containment, and long-term material compatibility [2,5,6].

Packed-bed TES (PBTES) systems are attractive for both sensible and latent heat storage because of their simple construction, modularity, and scalability. In these systems, the storage material forms a stationary bed, while a heat transfer fluid (HTF) moves through the voids between particles or capsules. For sensible heat storage, packed beds typically use low-cost, thermally stable solids such as rocks, ceramics, or mineral aggregates [6,7]. However, solid-packed beds generally have lower energy density than PCM-based systems and face operational challenges related to axial temperature gradients, flow distribution, and pressure drop.

An alternative approach is the use of encapsulated PCMs in packed-bed configurations. In this case, the PCM is enclosed in capsules to prevent leakage during melting and to enable direct convective heat transfer between the HTF and the capsule surface [8,9]. However, macroencapsulated PCM beds require careful design, as capsule geometry and material, PCM loading, bed porosity, and heat transfer fluid velocity significantly influence charging and discharging dynamics [10]. Encapsulation also adds thermal resistance, while corrosion, thermal stresses, and system integration remain key challenges for further development [11].

Recent studies highlight the potential of packed-bed LHS systems using nitrate salts and other PCMs. Cui et al. [11] reviewed multi-scale aspects of these systems, identifying material selection, encapsulation, corrosion resistance, thermal stresses, and system integration as key challenges. Costa et al. [12] developed a modular 100 kWh solar salt latent heat storage concept for integration with a small solar organic Rankine cycle plant, demonstrating that aluminum heat-transfer structures improve thermal response due to higher thermal conductivity. Han et al. [13] experimentally investigated a nitrate-salt-based latent heat TES unit and found that higher charging temperatures reduced melting time, while discharging was affected by heat losses and increased thermal resistance during PCM solidification. Wang et al. [14] studied a medium- and high-temperature packed-bed system with an encapsulated $NaNO_3$-KNO_3 nitrate salt, emphasizing both the promise of nitrate-based packed-bed LHS and the importance of accounting for flow resistance.

High-temperature PCM storage has been demonstrated at larger scales. Laing et al. [15] developed storage concepts using nitrate salts and highlighted the need for improved heat transfer. Johnson and Fiss [16] reported integrating a large-scale LHS system with a cogeneration plant to produce superheated steam. More recently, Li et al. [17] experimentally tested a 100 MJ cascaded packed-bed TES system with macroencapsulated PCMs, confirming that operating temperature significantly affects storage performance and heat recovery.

Packed-bed SHS systems have been extensively studied, especially for high-temperature waste-heat recovery and district heating. Jia et al. [18] conducted experimental and numerical studies on a 2 MWh rock-packed-bed thermocline storage system using basalt, demonstrating the feasibility of large-scale sensible heat storage for district heating. Touzo et al. [19] developed and tested a containerized packed-bed TES system for high-temperature waste heat recovery, using a bauxite-based ceramic material and air as the heat-transfer fluid, operating up to 525 °C. Their results confirmed the suitability of modular solid-media storage units at near-industrial scale. Ochmann et al. [20] examined packed-bed TES units using basalt particles of varying sizes and found that the tank aspect ratio influences energy and exergy efficiencies, as well as pressure losses. Collectively, these studies highlight the practical relevance of solid-packed-bed TES systems and em-

phasize the need to jointly consider thermal performance, pressure drop, geometry, and operating conditions.

Although both sensible- and latent-heat PBTES systems have been investigated in the literature, direct experimental comparisons between solid mineral storage materials and encapsulated nitrate-salt PCMs under similar operating conditions remain limited. Most published studies focus on a single storage mechanism, material group, numerical modelling, or component-level investigations, making it challenging to assess the practical trade-offs between SHS and LHS within the same TES unit. This gap is particularly important for medium- and high-temperature applications, where the selection of storage concepts must consider not only energy density but also charging and discharging dynamics, pressure drop, outlet heat losses, and thermal stratification. These bed-level phenomena are difficult to capture using only material-scale tests, single-capsule experiments, or numerical models.

To address these research gaps, this study experimentally compares sensible and latent heat storage performance in a laboratory-scale packed-bed TES unit at elevated temperatures. Basalt aggregate was selected as the reference sensible heat storage material, while a macroencapsulated PCM consisting of 60 wt.% $NaNO_3$ and 40 wt.% KNO_3 (solar salt) was used as the LHS material. Commercial aluminum containers were adapted for PCM encapsulation, providing a simple and practical solution with potential for future scale-up.

Experiments were conducted using a packed-bed TES unit with a packed-bed volume of approximately 25 L and containing up to 25 kg of PCM, with air as the heat transfer fluid. Charging and discharging tests were conducted at various mass flow rates and operating temperatures representative of medium and high-temperature thermal energy storage applications.

This study provides a comprehensive experimental evaluation of charging and discharging behavior, including temperature evolution, thermal power, stored and recovered energy, volumetric energy density, TES efficiency, air utilization efficiency, and specific thermal energy. By comparing basalt and macroencapsulated solar salt under similar conditions, this work provides practical design data and experimental insights into advantages and limitations of sensible and latent heat storage for packed-bed TES systems. Moreover, the knowledge gained is essential for selecting appropriate storage concepts for concentrated solar power, industrial waste-heat recovery, and other medium- and high-temperature thermal energy storage applications.

2. Materials and Methods

2.1. Sensible Heat Storage Material

Basalt aggregate was selected as the SHS material due to its high thermal stability, low cost, and abundance. Sieve analysis indicated that 77.42% of the sample mass fell within the 10.0–14.0 mm particle size range. The 14.0–20.0 mm fraction averaged 18.75%, while particles smaller than 10 mm were present only in trace amounts. Density (2.6–2.7 g/cm^3) and specific heat capacity values were taken from references [20,21].

The temperature dependence of basalt's specific heat capacity was considered in the energy calculations. As demonstrated in the experimental data reported by Hartlieb et al. [22], the specific heat capacity of basalt increases from slightly above 0.8 J g^{-1} K^{-1} at 100 °C to approximately 1.05 J g^{-1} K^{-1} at 400 °C. This range was considered in the energy calculations. The estimated bulk density was 1657 kg/m^3, with a porosity of 0.37.

2.2. Phase Change Material

A mixture comprising 60% sodium nitrate ($NaNO_3$) and 40% potassium nitrate (KNO_3), commonly referred to as solar salt, was selected as the PCM for LHS. This material

was chosen due to its low cost, good thermal stability, wide availability, and low toxicity, which are important for potential scale-up. Additional advantages include simple preparation without preliminary dehydration, relatively low hygroscopicity, lower corrosivity than chloride-based PCMs [6].

The PCM was prepared as follows. Potassium and sodium nitrate powders (KNO_3, 99.5% pure, $NaNO_3$ > 99%pure, Chemland, Stargard, Poland) were dried in an oven at 105 °C for 3 h, then pre-crushed using a laboratory blade mill (1300 W, 28,000 RPM, Chemland, Poland). The required quantities were weighed, mixed, and melted in a stainless-steel vessel in a muffle furnace at 350 °C. The molten PCM was then poured into aluminum bottles (Meping Europe Sp. z o.o., Stara Iwiczna, Poland), with a nominal capacity of 50 mL, a total volume of 65.5 mL, a diameter of 36 mm, and a height of 83 mm, ensuring sufficient space for thermal expansion. Before filling, the bottles were heated in an oven at 300 °C for 3 h to remove the protective varnish layer. After filling and cooling, the bottle necks were sealed using a 2-ton hand press. Each capsule contained approximately 100 g of solar salt. The estimated porosity was found to be 0.40, based on the volume of the PCM capsules and the packed bed.

The melting point and heat of fusion of the prepared PCM were determined using thermogravimetric analysis (TGA) with a Netzsch STA 409 PC Luxx differential thermal analyzer, (Netzsch Instrumenty Sp. z o.o., Kraków, Poland) which allows for simultaneous TG-DSC measurements. Samples of the PCM, previously melted, cooled, and ground into powder, were analyzed. The heating rate was set at 10 K/min, and the measurements were performed in an argon atmosphere. The heat of fusion was determined as the average of at least two measurements. Results are shown in Figure 1 and Table 1. The measured thermophysical properties were consistent with values reported in the literature.

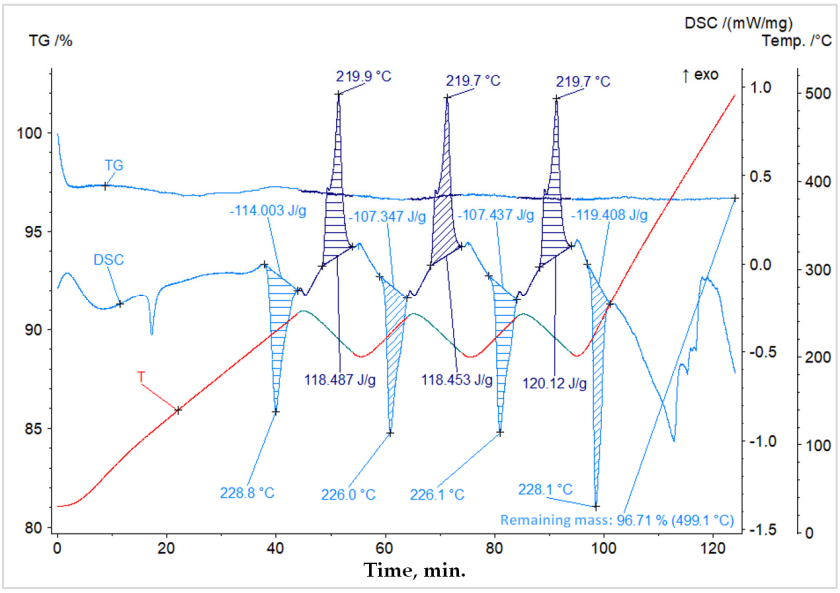


Figure 1. TG−DSC analysis of prepared phase change material (solar salt).

Table 1. Parameters of studied PCM.

PCM Composition	Melting Point, °C	Heat of Fusion kJ/kg	Specific Heat Capacity, J/g·K	Density, kg/m^3	Thermal Conductivity, W/m	Source
60% $NaNO_3$ 40% KNO_3	220–223	113–117	Solid: 1.58–1.60	1710 (at 565 °C)	0.55	[23,24]
	221 solidification 238 start of crystallization	161 (based on the average of heat fusion of each component)	Liquid: 1443 + 0.172 × T (°C)	Liquid: 2090 − 0.636 × T (°C)	Liquid: 0.443 + 1.9 × 10−4 × T (°C)	[25]
	226–228 (melting) 219.7–219.9 (solidification)	118.5–120.1 (solidification) 107.3–119.4 (melting)	-	-	-	This work

The TGA indicated a mass loss of 3.29%, with most of the weight loss occurring below 50 °C due to water evaporation. The absorbed water was likely introduced during sample preparation under ambient conditions and intensified by the hygroscopic nature of sodium nitrate. No significant mass changes were observed at higher temperatures, confirming the thermal stability of the investigated PCM up to 500 °C.

To further assess thermal stability, 20 g of PCM was placed in a 100 mL beaker and heated in an electric oven from 300 to 500 °C, maintaining each temperature (300, 400, and 500 °C) for 2 h. The tests were conducted in an open vessel to allow gas release. After each interval, the beaker was weighed to determine mass loss. Following the final heating at 500 °C, the total mass loss remained below 0.5%.

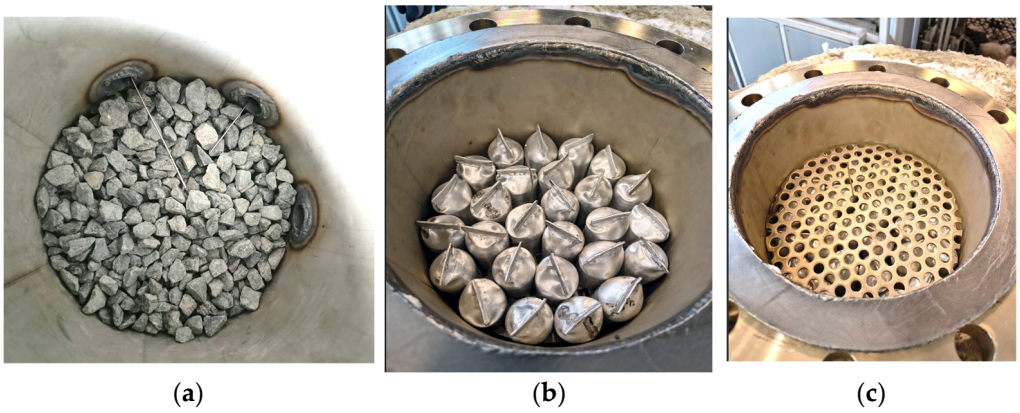
2.3. Thermal Energy Storage Test Rig

The Institute of Energy and Fuel Processing Technology (ITPE) developed and constructed a test rig to study TES in a fixed bed, as shown in Figure 2. The main component is a steel column (TES unit), 1 m long, with a 215 mm internal diameter and 2 mm wall thickness, capable of holding about 25 dm^3 of storage material. The packed bed is 0.7 m high, giving an aspect ratio of 3.25. Figure 3 shows the tested materials (basalt and encapsulated PCM) inside the TES unit. The unit contained either approximately 42 kg of basalt aggregate or 25 kg of PCM (243 bottles).



Figure 2. A view of the thermal energy storage test rig in ITPE (Zabrze, Poland).

The TES column is insulated with 100 mm of high-temperature quartz wool and 100 mm of high-temperature mineral wool. The test rig is fully instrumented, with a focus on temperature measurements using K-type thermocouples placed at various axial and radial positions within the TES bed. Figure 4 shows the temperature measurement locations within the TES unit.



(**a**) (**b**) (**c**)

Figure 3. Filling the TES unit with thermal storage material, (**a**) basalt aggregate, (**b**) encapsulated solar salt, and (**c**) air distributor.

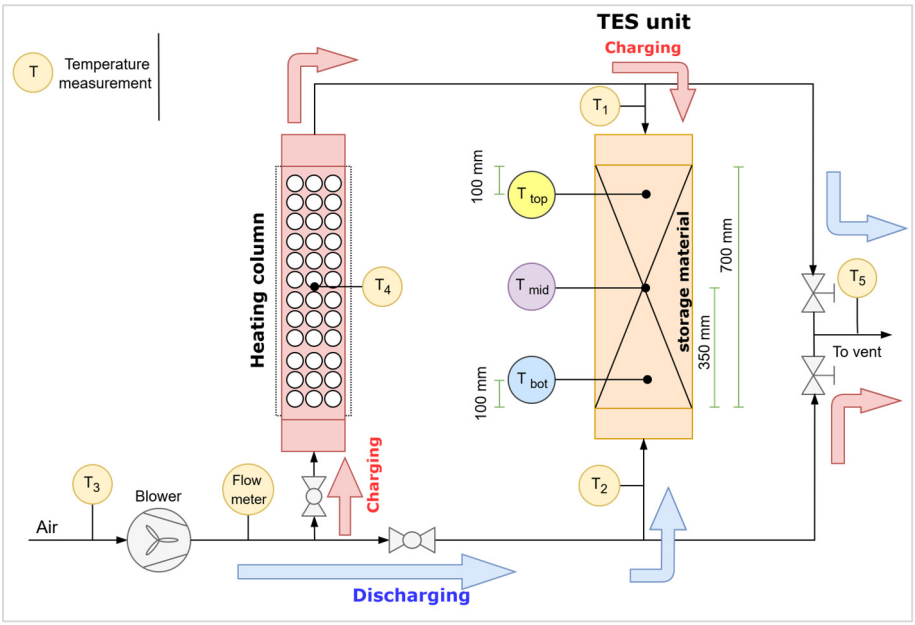


Figure 4. A schematic diagram of the test rig used in this study.

The symbols T top, T mid, and T bot denote the average temperatures measured in the upper, middle, and lower sections of the packed bed, respectively. At each measurement level, the temperature was calculated as the arithmetic mean of two thermocouple readings: one recorded along the central axis of the TES unit and the other measured 50 mm from the axis. This approach provided a more representative assessment of the thermal state of the packed bed.

Temperature and air flow rate were continuously monitored and recorded throughout the experiments. The air flow rate was measured using a VA 420 flow meter (CS Instruments Polska Sp. z o.o., Łódź, Poland) based on the calorimetric measuring principle.

The accuracy of the instruments used and the uncertainties of the calculated parameters are presented in Table 2. The standard uncertainty of temperature measurement was estimated from the accuracy of the K-type thermocouples, while the uncertainty of the air mass flow rate was determined from the flow meter accuracy specified by the manufacturer. The relative standard uncertainties of the derived parameters, including supplied and recovered energy, average thermal power, energy density, storage efficiency, air utilization efficiency, and specific thermal energy, were calculated using the root-sum-square uncertainty propagation method.

Table 2. Accuracy of used instruments and uncertainties of key parameters.

Parameter/Instrument	Symbol	Unit	Accuracy	Standard Uncertainty
Temperature. Thermocouple type K, length 500 mm. RS Pro.	T	°C	±1.5 °C or ±0.4% of the measured value	±0.87 °C
Air flow rate. Flow meter VA 420. CS instruments.	$\dot{m}_{air}$	kg/h	±1.5% of the measured value plus ±0.05% of the full-scale range.	±1.36 kg/h, for flow rate of 120 kg/h, u_r: 1.1–1.4%
Energy stored/recovered Average power	Q_{in}/Q_{out} P_{avg}	kJ kW	-	u_r: 1.55–1.90%
Energy density	E_v	MJ/m^3	-	u_r: 1.93–2.21%
TES efficiency	η_{TES}	%	-	u_r: 2.20–2.68%
Charging/discharging efficiency	η_{ch}, η_d,	-	-	u_r: 2.30–3.89%
Air utilization efficiency	η_{air}	-	-	u_r: 2.18–2.46%
The specific outlet thermal energy/recovered thermal energy	q_{out}/q_{rec}	kJ/kg_{air}	-	u_r: 1.92–2.35%

u_r—relative standard uncertainty.

Moreover, to verify the repeatability of the experimental procedure, the charging experiment was repeated under identical operating conditions. As shown in Figure S1 (Supplementary Materials), the temperature profiles at all three measurement locations exhibited very good agreement, confirming the repeatability and reliability of the experimental methodology.

2.4. Experimental Procedure

A fixed air flow from a blower, regulated by a frequency inverter, was heated in a steel pipe heating column equipped with band heaters totaling 15 kW (Conductance S.J. Kuczera, Topola-Osiedle, Poland). To enhance heat transfer, the column was filled with 25-mm alumina balls (99% Al_2O_3, Hurtgral, Swarzędz, Poland). The 15 kW value represents the nominal installed heating power of the heating column; however, the instantaneous heating power was not constant during charging because the column was controlled by the PID regulator Lumel RE81 (Lumel S.A., Zielona Góra, Poland) and adjusted to the required inlet-air temperature under each air flow condition. The set temperature in the heating column was higher than the target TES unit temperature to compensate for heat losses and limited heat transfer.

Heated air from the column entered the TES unit and flowed downward through the TES material (basalt or PCM capsules). Seven thermocouples monitored temperatures at various points in the bed. In the PCM study, additional measurements were taken inside the PCM bottle at the upper and middle sections of the column.

The packed bed was gradually heated until the average packed-bed temperature reached the target value (150 °C, 290 °C, or 330 °C). Uniform temperature throughout the bed could not be achieved; a temperature difference of up to 10 °C between the bottom and top was observed. As heating continued, the local heat transfer intensity decreased, thereby increasing the time required for uniform temperature distribution. Heat losses to the surroundings and limited effective thermal conductivity further contributed to this effect.

During the discharging phase (cooling the bed), the valves were adjusted so that the fixed air flow from the blower bypassed the heating column and flowed upward through the TES unit. Discharging continued until the bed reached a steady-state temperature, as in the charging phase.

Table 3 presents the experimental conditions for sensible and latent heat storage tests. The average bed temperature was calculated as the arithmetic mean of the temperatures measured at the top, middle, and bottom of the TES unit.

Table 3. Experimental conditions of the TES experiments.

Test	Target Air Flow Rate, kg/h	Target Packed-Bed Temperature	Average Packed-Bed Temperature, °C	Storage Type
B1	60	150	158	SHS
B2	90	150	147	
B3	120	150	155	
B4	60	290	284	
B5	90	290	284	
B6	120	290	285	
B7	60	330	340	
B8	90	330	330	
B9	120	330	334	
S1	60	290	305	LHS
S2	90	290	288	
S3	120	290	294	
S4	60	400	400	
S5	120	400	382	

It should be noted that the target packed-bed temperature represents the nominal operating condition, whereas the average packed-bed temperature listed in Table 3 corresponds to the experimentally obtained value at the end of charging. Small deviations from the target temperature resulted from axial temperature gradients, heat losses to the surroundings, limited effective thermal conductivity of the packed bed, and the decreasing heat-transfer driving force near the end of charging.

2.5. Calculated Parameters of TES

Based on the recorded temperature and air flow measurement data, the energy storage parameters were calculated. The total energy supplied to the TES unit during charging (Q_{in}, kJ) was determined as:

$$Q_{in} = \sum_{i=1}^{N} \dot{m}_{air} C_{p\ air} (T_1 - T_2)_i \Delta t_i \quad (1)$$

where $\dot{m}_{air}$ is the air mass flow rate (kg/s) and C_{pair} is the temperature-dependent specific heat capacity of air (J/kg·K) determined using a polynomial fit based on tabulated thermophysical data. Temperatures T_1 and T_2 (°C) are the inlet and outlet air temperatures, respectively, as indicated in Figure 4. During charging, $T_1 > T_2$. The time interval between two consecutive measurements is denoted by Δt_i (s), while N denotes the number of recorded data points from the beginning of the charging until the target average packed-bed temperature was reached.

The energy recovered (Q_{out}, kJ) during the discharging was calculated analogously:

$$Q_{out} = \sum_{i=1}^{N} \dot{m}_{air} C_{p\ air} (T_2 - T_1)_i \Delta t_i \quad (2)$$

In this case, $T_2 > T_1$. N denotes the number of recorded data points from the beginning of discharging until the average packed-bed temperature is close to ambient temperature.

The average thermal power (kW) P_{avg} during charging was calculated as:

$$P_{avg} = \frac{Q_{in}}{t_{char}} \quad (3)$$

And for discharging:

$$P_{avg} = \frac{Q_{out}}{t_{disch}} \quad (4)$$

where t_{char}/t_{disch} are the total charging or discharging time, respectively (s).

TES efficiency (%) was defined as:

$$\eta_{TES} = \frac{Q_{out}}{Q_{in}} \cdot 100\% \quad (5)$$

This parameter evaluates the thermal performance of the storage unit based solely on the ratio of recovered to supplied thermal energy. It does not include the electrical energy consumption of auxiliary equipment, such as the blower, heaters, or control system.

Theoretical energy stored or recovered as sensible heat (Q_S, kJ), based on material level, was calculated as:

$$Q_S = m_b \overline{C}_{pb} \Delta T_{TES} \quad (6)$$

where m_b is the mass of the basalt packed bed (kg), $\overline{C}_{pb}$ is the mean specific heat capacity of basalt over the considered temperature interval (kJ/kg·K^{-1}), and ΔT_{TES} (°C) is the difference between final (T_f) and the initial average packed-bed temperatures (T_i). The value of $\overline{C}_{pb}$ was approximated using the specific heat capacity evaluated at the mean temperature of the considered interval.

Theoretical energy stored in PCM (Q_{PCM}, kJ) was calculated as follows:

$$Q_{pcm} = m_{pcm}\left[C_{ps}(T_m - T_i) + H_f + C_{pl}(T_f - T_m)\right] + m_C C_{pC}(T_f - T_i) \quad (7)$$

where m_{pcm} is the mass of PCM (kg), H_f is the heat of fusion (kJ/kg), C_{ps}, C_{pl} are the specific heat capacities of solid and liquid PCM, respectively (kJ/kg·K), T_m is the melting temperature (°C), T_i and T_f are initial and final PCM temperatures, respectively (°C), m_C is the mass of shell capsules, and C_{pC} is the specific heat capacity of aluminum. A value of 1.56 J/kg·K was assumed for C_{ps}, and C_{pl} was estimated based on correlation from [25].

The charging and discharging efficiencies were introduced to evaluate the consistency between the air-side energy balance and the energy stored in or recovered from the storage material. The charging efficiency was calculated as:

$$\eta_{ch} = \frac{(Q_s \text{ or } Q_{pcm}) + Q_{st}}{Q_{in}} = \frac{(Q_s \text{ or } Q_{pcm}) + m_{st}\overline{C}_{p_{st}}\Delta T_{st}}{Q_{in}} \quad (8)$$

and discharging efficiency was calculated as:

$$\eta_d = \frac{Q_{out}}{(Q_s \text{ or } Q_{pcm}) + Q_{st}} \quad (9)$$

where Q_{st} (kJ) is the energy stored/recovered in the steel structure of the TES unit ($m_{st}\overline{C}_{p_{st}}\Delta T_{TES}$), m_{st} is mass of the TES steel structure, and $\overline{C}_{p_{st}}$ is the mean specific heat capacity of steel. Q_s and Q_{pcm} are used for calculating charging/discharging efficiency for SHS or LHS, respectively.

Higher η_{ch} indicates more effective transfer of thermal energy from the air stream to the storage bed, and η_d describes the fraction of the thermally available energy in the bed that was recovered during discharging.

Energy density (E_v, MJ/m^3), based on storage material level, was calculated using the following formula:

$$E_v = \frac{Q_{in} - Q_{st}}{V_{bed}} \quad (10)$$

where V_{bed} is the packed-bed volume (0.0254 m^3). The same approach was applied for both charging and discharging.

Parameter q_{out} (specific outlet thermal energy) represents the average amount of thermal energy carried by 1 kg of air leaving the TES unit above ambient temperature (kJ/kg$_{air}$) during charging:

$$q_{out} = \frac{\sum_{i=1}^{N} \dot{m}_{air} C_{p\ air} (T_2 - T_{amb})_i \Delta t_i}{\sum_{i=1}^{N} \dot{m}_{air} \Delta t_i} \quad (11)$$

T_{amb} is the ambient temperature (°C). This parameter may be interpreted as a measure of outlet thermal losses.

Similarly, for the discharging process, a specific heat recovery q_{rec} (kJ/kg$_{air}$) was introduced to determine the energy recovered per kilogram of air leaving the TES unit.

$$q_{rec} = \frac{\sum_{i=1}^{N} \dot{m}_{air} C_{p\ air} (T_2 - T_1)_i \Delta t_i}{\sum_{i=1}^{N} \dot{m}_{air} \Delta t_i} = \frac{Q_{out}}{\sum_{i=1}^{N} \dot{m}_{air} \Delta t_i} \quad (12)$$

To evaluate the fraction of the thermal energy carried by the air stream that was effectively transferred to the TES unit during charging, the air utilization efficiency, η_{air} was defined as:

$$\eta_{air} = 1 - \frac{q_{out}}{q_{in}} = \frac{\sum_{i=1}^{N} \dot{m}_{air} C_{p\ air} (T_1 - T_2)_i \Delta t_i}{\sum_{i=1}^{N} \dot{m}_{air} C_{p\ air} (T_1 - T_{amb})_i \Delta t_i} \quad (13)$$

where q_{in} represents the specific thermal energy available in the inlet air stream above ambient temperature. For these calculations, the specific heat of air was evaluated as an average value over the corresponding temperature range, i.e., (T_1–T_2) and (T_1–T_{amb}), respectively.

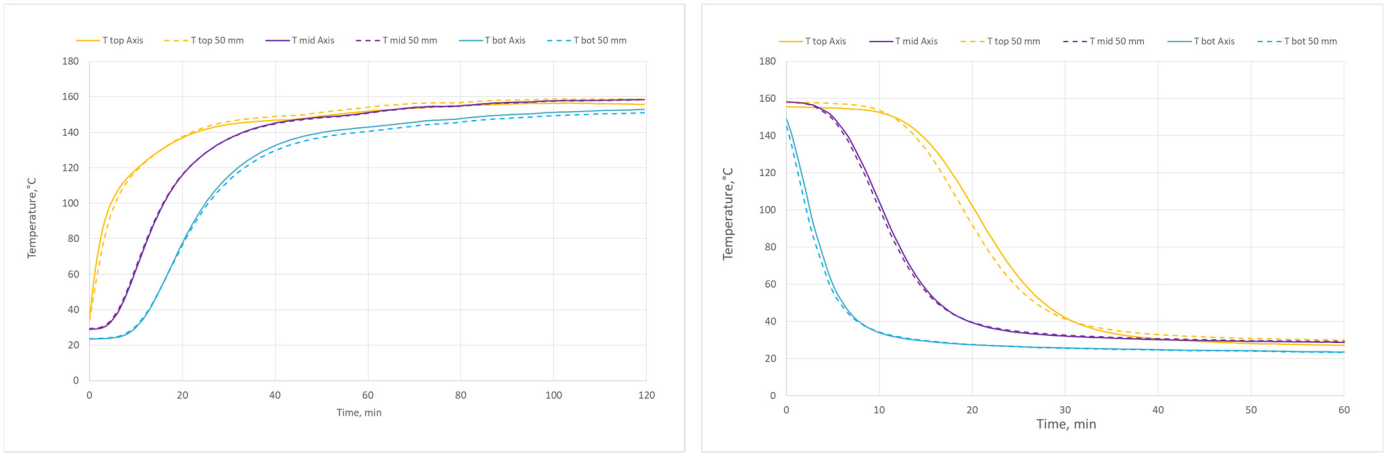
3. Results

The results obtained from the thermal energy storage experiments are presented in this section. In the SHS tests, basalt aggregate was heated to the target packed-bed temperatures of 150 °C, 290 °C, and 330 °C. The effect of air flow rate on charging and discharging performance was examined at 60, 90, and 120 kg/h.

For clarity, this section presents only the most representative results. Additional results are provided in Appendix A or in Supplementary Materials, as referenced in the text.

3.1. Sensible Heat Storage Performance

Basalt aggregate was used as the reference sensible heat storage material. Before evaluating the effects of air flow rate and packed-bed temperature, the representativeness of the averaged axial bed temperatures was verified by comparing temperature measurements along the column axis with those recorded 50 mm from the axis, as shown in Figure 5 (T top 50 mm, T mid 50 mm, and T bot 50 mm).



(**a**) (**b**)

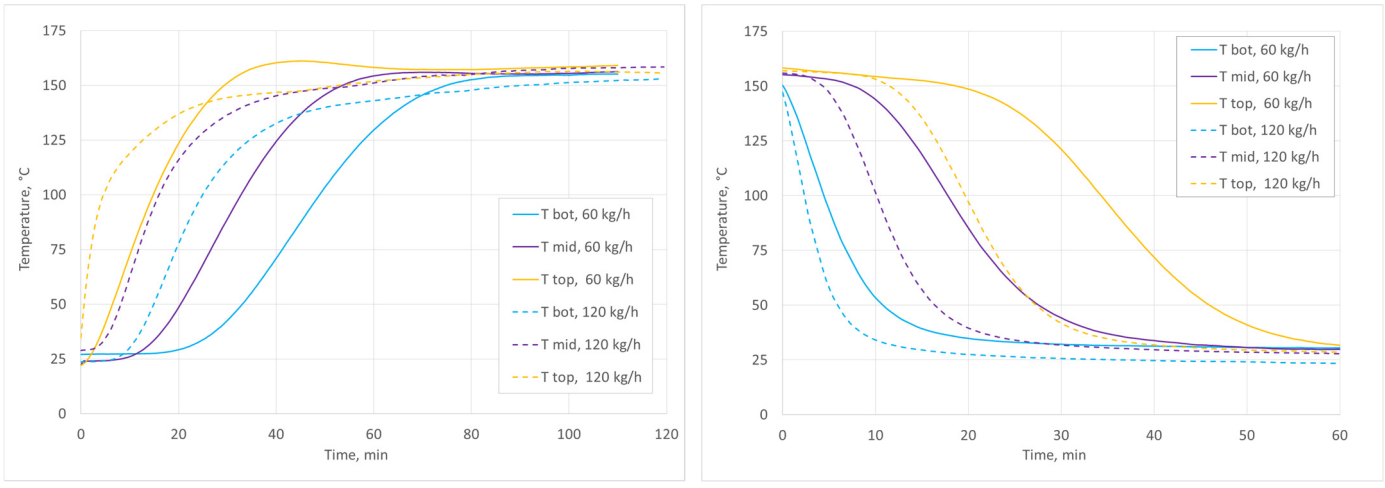
Figure 5. Temperature profile in the TES unit along the column axis and 50 mm from the axis for (**a**) charging and (**b**) discharging. Air flow rate of 120 kg/h.

Figure 5 presents a typical temperature profile during charging and discharging. The close agreement between temperatures measured along the column axis and at 50 mm away from the axis indicates negligible radial temperature gradients in the central region of the packed bed. Although temperatures were not measured directly adjacent to the wall, the results indicate that the chosen measurement locations adequately represent the bulk thermal behavior of the packed bed.

Additional temperature profiles for other air flow rates and temperatures are provided in Appendix A (Figures A1 and A2).

3.1.1. Effect of Air Flow Rate

Figure 6 presents axial temperature profiles in the basalt-packed bed during charging and discharging at air flow rates of 60 and 120 kg/h. The temperature profiles for test B2 (90 kg/h) are provided in Appendix A (Figure A3) for clarity.



(**a**) (**b**)

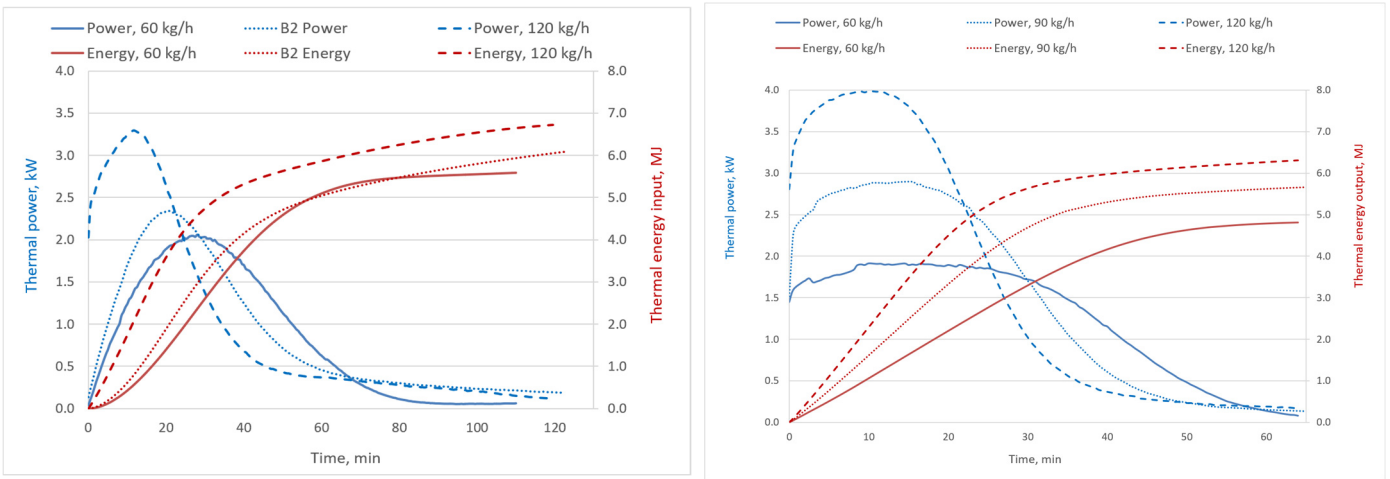
Figure 6. Comparison of axial temperature profiles for air flow rates of 60 kg/h and 120 kg/h during (**a**) charging and (**b**) discharging of the basalt packed bed. Target packed bed temperature of 150 °C.

Figure 6 shows a steady temperature increase along the TES column axis for both air mass flow rates during charging, indicating the propagation of the heating front from the hot-air inlet. The temperature rises fastest near the inlet (T top), then at the middle (T

mid), and slowest at the bottom (T bot), which is farthest from the heat source. Increasing the air mass flow rate from 60 kg/h to 120 kg/h generally accelerated the propagation of the heating front, as indicated by the reduced time delay between measurement locations. However, the transient inlet air temperature was not identical in these two experiments due to the dynamic response of the heating column (Figure S2). Consequently, the faster temperature increase observed in the upper section of the bed was influenced by the air flow rate and inlet air temperature profile. The general influence of air flow rate is further confirmed by the experiments performed at higher packed-bed temperatures (Figure A4), where the same trend of faster thermal-front propagation with increasing air flow rate was observed under comparable operating conditions.

At the end of charging, both conditions stabilize at a bed temperature of about 150–155 °C. The lower air flow rate of 60 kg/h results in smaller axial temperature differences, indicating more uniform heating due to longer gas–solid contact time, thereby promoting temperature equalization within the storage bed.

During discharging, the TES unit shows a reverse thermal response (Figure 6b). At an air flow rate of 120 kg/h, the packed bed cools much faster across all measurement zones, particularly in the lower section directly exposed to incoming cold air. In contrast, a lower air flow rate of 60 kg/h results in a more gradual temperature decrease and smaller axial temperature differences throughout most of the process. Increasing the air flow rate thus accelerates both charging and discharging, resulting in more pronounced axial temperature gradients within the packed bed. Figure 7 presents the thermal power and energy input/output profiles during charging and discharging of the TES unit at various air flow rates. During charging, thermal power initially rises, peaks, and then declines as the temperature difference between the inlet air and the packed bed decreases. At 120 kg/h, maximum thermal power occurs sooner and reaches about 3.3 kW, compared to approximately 2.0 kW at 60 kg/h. This trend aligns with the faster temperature response shown in Figure 6a.



(**a**) (**b**)

Figure 7. Thermal power and thermal energy input/output during (**a**) charging and (**b**) discharging, depending on air flow rates (60–120 kg/h). Target packed bed temperature of 150 °C.

Thermal energy input increases continuously throughout the charging at all air flow rates. While final packed-bed temperatures are similar, higher air flow rates deliver more thermal energy. This suggests that the air stream supplies additional energy during charging, but not all is effectively stored in the packed bed. The discrepancy likely results from increased outlet heat losses and heat accumulation in the TES unit's structural components

at higher air flow rates. Section 3.1.3 provides a detailed comparison of supplied, stored, and recovered thermal energy.

During discharging, higher air flow rates increase thermal power output and shorten the discharging duration. The maximum output is about 4 kW at 120 kg/h, with lower values at 90 kg/h and 60 kg/h. Cumulative recovered thermal energy increases rapidly at first, then levels off as the packed-bed temperature decreases. Although higher air flow rates yield greater instantaneous power, total recovered energy does not increase proportionally. This suggests that faster discharging improves the heat recovery rate but may reduce the effective use of stored heat. Section 3.1.3 further quantifies these effects. Additional power and energy plots for tests B4–B9 are provided in Appendix A, Figure A5.

3.1.2. Effect of Packed Bed Temperature

The effect of packed-bed temperature under constant air flow was evaluated at an air flow rate of 60 kg/h, as this condition clearly distinguishes the thermal power and energy input profiles across different charging temperatures. Results for higher air flow rates (90 and 120 kg/h) are presented in Appendix A (Figures A6–A9). These results show a similar trend, although the differences in power profiles during charging are less pronounced due to intensified convective heat transfer at higher air flow rates.

Figure 8 shows the effect of packed-bed temperature on the thermal behavior of the TES unit at a constant air flow rate of 60 kg/h. During charging, temperature increases sequentially from the upper to the lower section, indicating the movement of the thermal front from the hot-air inlet. Raising the target packed-bed temperatures to 290 °C and 330 °C increases the separation among T top, T mid, and T bot, reflecting stronger axial temperature gradients at higher operating temperatures. At 150 °C, the temperature profiles are closer together, indicating a more uniform thermal state.

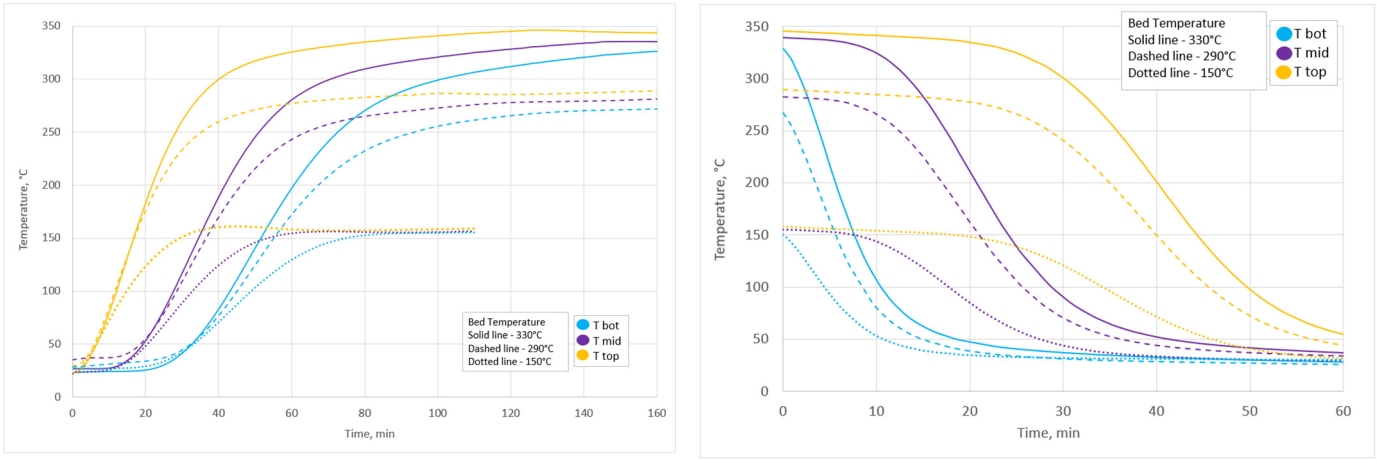
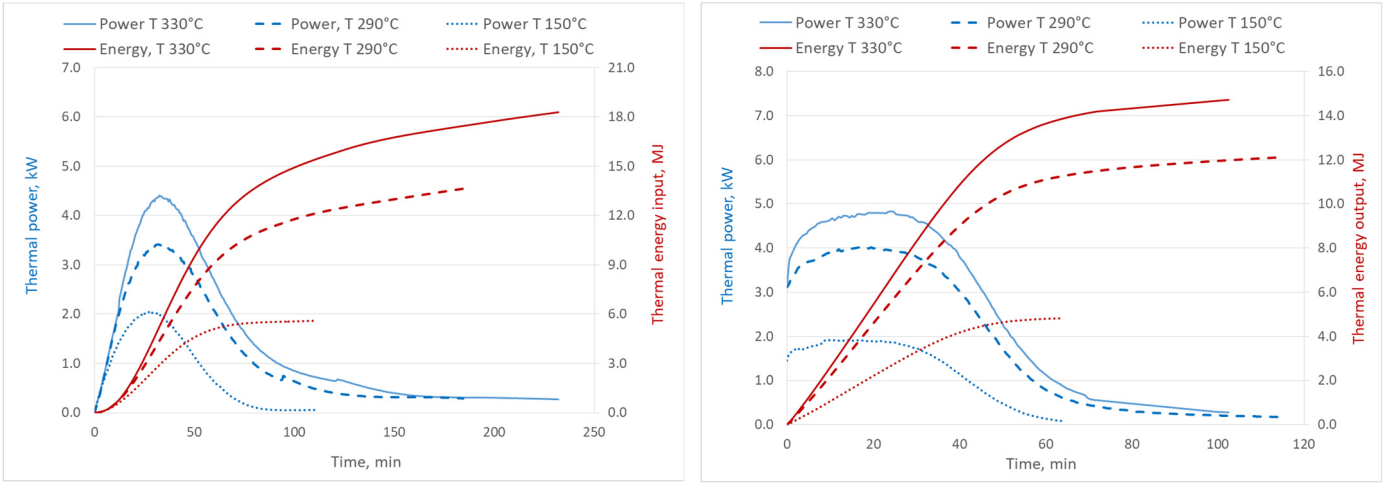


Figure 8. Temperature profiles of TES unit depending on bed temperature; (**a**) charging and (**b**) discharging. Air flow rate of 60 kg/h.

During discharging, cooling occurs in the opposite direction: the lower section cools first, while the upper section retains heat longer. Axial temperature differences are more pronounced at higher initial bed temperatures, confirming that the TES unit becomes more thermally stratified at elevated temperatures. Similar trends were observed at higher air flow rates, as shown in Appendix A (Figures A6 and A7), demonstrating that packed-bed temperature consistently affects axial temperature distribution across different flow conditions.

Figure 9 presents the thermal power and energy profiles. Higher packed-bed temperatures resulted in greater peak thermal power and increased thermal energy input during

charging. This can be attributed to the greater temperature difference between the inlet air and the packed bed, which increases the heat-transfer driving force. However, the increase in thermal energy input was not directly proportional to the rise in target bed temperature, as higher operating temperatures also enhanced instantaneous heat transfer and increased heat losses from the TES unit.



(**a**) (**b**)

Figure 9. Thermal power and energy profiles of the TES unit depending on packed-bed temperature; (**a**) charging and (**b**) discharging. Air flow rate of 60 kg/h (tests B1, B4, B7).

During discharging, higher initial packed-bed temperatures resulted in greater thermal power output and increased recovered energy. The 330 °C test produced the highest power output and recovered energy, followed by the 290 °C and 150 °C tests. This demonstrates that higher initial bed temperatures provide a stronger driving force for convective heat recovery, especially at the start of discharging. However, increases in recovered energy and discharging duration were not proportional to the rise in initial bed temperature, since the heat recovery rate also increased at higher temperatures. Thus, packed-bed temperature influences both the total stored sensible heat and the rate at which heat can be supplied to and recovered from the TES unit.

3.1.3. Thermal Energy Storage and Recovery Analysis

Table 4 presents the results of charging the TES unit using sensible heat storage (tests B1–B9). To assess whether increased air flow improves heat transfer to the packed bed, the parameters q_{out} and η_{air} were calculated using Equations (11) and (13). A higher q_{out} indicates greater heat loss with the outlet air. The air utilization efficiency, ηair, measures the proportion of thermal energy from the inlet air transferred to the TES unit. Higher ηair values indicate more effective heat transfer from the air to the TES unit.

It should be noted that these parameters were calculated up to a predefined average packed-bed temperature to exclude the final asymptotic stage of charging, when bed temperature increases are minimal, and outlet heat losses may rise significantly. The selected average packed-bed temperatures were 140 °C for tests B1–B3, 270 °C for tests B4–B6, and 300 °C for tests B7–B9.

The results show that specific outlet thermal energy q_{out} generally increased with higher air flow rates, especially at elevated charging temperatures. In tests B4–B6, q_{out} rose from 93 to 174 kJ/kg_{air}, and in B7–B9, from 73 to 171 kJ/kg_{air}. Conversely, η_{air} decreased as air flow rate increased, particularly at the highest rates. For example, η_{air} decreased from 0.58 to 0.22 in B4–B6 and from 0.70 to 0.31 in B7–B9. These findings indicate that higher air flow rates accelerated charging but reduced the effective use of thermal energy

in the air stream. The increase in q_{out} and the decrease in η_{air} suggest an earlier thermal breakthrough and a shorter air residence time in the packed bed.

Table 4. Results of charging TES unit (basalt packed-bed).

Test	$m_{air\ avg}$, kg/h	T_{avg}, °C	P_{avg}, kW	Q_{in}, MJ	η_{ch}	E_v, MJ/m^3	q_{out}, kJ/kg$_{air}$	η_{air}
B1	60	158	0.85	5.59	1.24	132	25	0.79
B2	88	146	0.83	6.08	0.97	162	26	0.40
B3	119	155	0.94	6.73	1.01	176	43	0.62
B4	58	283	1.23	13.62	1.02	353	93	0.58
B5	88	284	1.45	15.93	0.91	436	108	0.51
B6	118	285	1.24	15.34	0.90	422	174	0.22
B7	59	340	1.31	18.29	0.96	487	73	0.70
B8	87	329	1.52	18.23	0.91	498	89	0.64
B9	105	334	1.64	19.07	0.90	524	171	0.31

$m_{air\ avg}$—average air flow rate and T_{avg}—average packed-bed temperature at the final stage of charging.

This trend is also evident in the charging efficiency η_{ch}. Although η_{ch} remained near unity in most tests, it generally decreased as air flow rate increased within each temperature series. For B4–B6, η_{ch} fell from 1.02 to 0.90, and for B7–B9, from 0.96 to 0.90. This indicates that higher air flow rates led to less effective retention of air-side energy in the storage material. Values slightly above unity in some tests are due to experimental uncertainty and assumptions in the energy-balance calculations, given a relative standard uncertainty of approximately 2–4%. Moreover, the unusually high value of η_{ch} for test B1 should be interpreted with caution. No clear experimental cause for this deviation was identified, and the result is likely due to the greater sensitivity of the energy balance under low-temperature and low-air flow-rate operating conditions.

A slight deviation from the general trend was observed in test B2, which showed a lower η_{air} than B3 despite a lower q_{out}. The experimental records, including the heating-column temperature and the inlet-air temperature, were rechecked, and no clear operational error was identified. As shown in Figure A10, B2 reached a significantly lower average packed-bed temperature than B1 and B3. Therefore, this deviation is most likely related to the specific transient thermal profile of B2 rather than to the air flow rate alone. Consequently, this result should be interpreted with caution.

A comparison of P_{avg}, Q_{in}, and E_v shows that higher air flow rates increased charging power but did not necessarily enhance effective energy storage. Volumetric energy densities depended mainly on the achieved packed-bed temperature, increasing from 132–176 MJ/m^3 in B1–B3 to 487–524 MJ/m^3 in B7–B9. The final thermal state of the basalt bed primarily determined energy density, while air flow rate mainly influenced charging dynamics and the distribution of supplied energy among storage, outlet heat losses, and structural heat accumulation.

Table 5 summarizes the discharging process results. The specific recovered thermal energy (q_{rec}), defined in Equation (12), represents the average thermal energy recovered per kilogram of air. Higher q_{rec} values indicate more effective heat recovery per unit mass. Discharging efficiency (η_d) quantifies the proportion of the bed's available thermal energy that was recovered.

Table 5. Results of discharging TES unit (basalt packed-bed).

Test	$m_{air\ avg}$, kg/h	T_{avg}, °C	P_{avg}, kW	Q_{out}, MJ	η_d	E_v, MJ/m^3	q_{rec}, kJ/kg$_{air}$	η_{TES}, %
B1	61	155	1.25	4.81	0.74	108	74	86.1
B2	90	146	1.53	5.63	0.89	139	43	92.5
B3	120	153	1.64	6.30	0.93	160	17	93.7
B4	62	280	1.76	12.10	0.87	293	103	88.9
B5	92	283	2.34	13.53	0.95	345	92	84.9
B6	120	282	3.45	13.05	0.95	332	104	85.1
B7	61	338	2.39	14.72	0.85	351	142	80.5
B8	90	323	2.69	15.80	0.95	402	107	86.7
B9	121	330	3.98	15.88	0.95	405	118	83.3

$m_{air\ avg}$—average air flow rate and T_{avg}—average packed-bed temperature at the start of discharging process.

Average discharging power increased (P_{avg}) with higher air flow rates across all temperature ranges. In the low-temperature series (B1–B3), P_{avg} rose from 1.25 to 1.64 kW as the air flow rate increased from 61 to 120 kg/h. At higher packed-bed temperatures, P_{avg} increased from 1.76 to 3.98 kW. These results demonstrate that increasing air flow rate enhances convective heat transfer and accelerates thermal energy recovery from the TES unit. This effect is more pronounced at higher packed-bed temperatures due to the greater temperature difference between the storage material and the heat-transfer fluid. This trend is consistent with the heat-transfer relationship ($Q = \dot{m}C_p\Delta T$), where a higher mass flow rate increases the rate of thermal energy transfer and the achievable discharging power.

However, q_{rec} did not increase proportionally with air flow rate. In the low-temperature series (B1–B3), q_{rec} decreased from 74 to 17 kJ/kg$_{air}$ as the air flow rate increased from 61 to 120 kg/h. This indicates that, although total recovered energy and average discharging power increased, each kilogram of air recovered less heat due to shorter residence time in the packed bed. A similar trend occurred in the high-temperature series (B7–B9), where q_{rec} decreased from 142 kJ/kg$_{air}$ at 61 kg/h to 107–118 kJ/kg$_{air}$ at higher air flow rates. In contrast, for the intermediate-temperature series (B4–B6), q_{rec} remained between 92 and 104 kJ/kg$_{air}$, suggesting that the air flow rate had less impact on heat recovery per unit mass in this range.

Recovered thermal energy (Q_{out}) and energy density (E_v) increased with higher initial packed-bed temperatures. The lowest Q_{out} and E_v values were observed for B1–B3, while the highest values occurred in the high-temperature series B7–B9, reaching approximately 15.8–15.9 MJ and 351–405 MJ/m^3, respectively. In turn, the heat recovered from the basalt-packed bed averaged 65% of the total recovered heat. These results confirm that discharging performance is primarily determined by the initial thermal state of the basalt-packed bed.

Discharging efficiency, η_d, ranged from 0.74 to 0.95. In most tests, η_d was close to or above 0.85, indicating that a large fraction of the available thermal energy was recovered. The highest values, around 0.95, were observed in several intermediate- and high-temperature tests, confirming effective heat extraction from the basalt-packed bed. Lower values, particularly for B1 and B7, may be attributed to non-uniform residual temperature distribution, heat retained in structural components, and unavoidable thermal losses during the transition between charging and discharging.

TES efficiency (η_{TES}) ranged from 80.5% to 93.7%, indicating that a significant fraction of stored energy was recovered during discharging. These high values confirm the effective operation of the TES unit. The highest efficiencies were observed in the low-temperature series, particularly for B2 and B3, where η_{TES} reached 92.5% and 93.7%, respectively. At higher packed-bed temperatures, η_{TES} remained high, typically between 80% and 89%. This

decrease may result from increased heat losses to the surroundings and greater thermal inertia of structural components at elevated temperatures. Before discharging, the air flow path was reconfigured by adjusting the gate valves, a process that typically took 2–3 min. During this operation, some stored heat was lost to the surroundings and redistributed within the TES unit. As a result, the average packed-bed temperature at the start of discharging was slightly lower than the maximum temperature reached at the end of charging, with this effect more pronounced at higher bed temperatures.

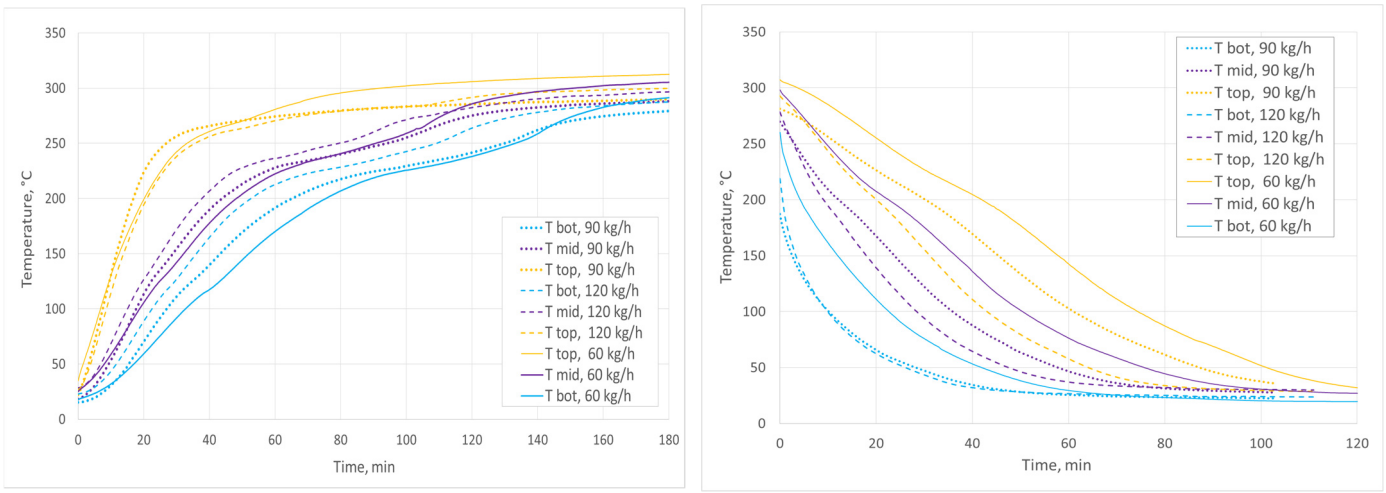
Moreover, due to practical time constraints, the packed bed was not fully cooled to ambient temperature during discharging. As a result, residual heat remained in the basalt bed and structural components, which explains the lower value of η_{TES}.

3.2. Latent Heat Storage Performance

After the sensible heat storage tests, the TES unit was filled with encapsulated solar salt to evaluate the thermal behavior of the latent heat storage configuration. The analysis focuses on the temperature response of the PCM bed and capsules, followed by the corresponding thermal power, energy storage, and recovery characteristics. A direct comparison between the basalt and encapsulated solar salt beds is presented separately in Section 3.3.

3.2.1. Temperature Profiles

Figure 10 shows the thermal response of the TES unit filled with encapsulated solar salt during charging and discharging at different air flow rates.



(**a**) (**b**)

Figure 10. Comparison of axial temperature profiles for air flow rates of 90 kg/h and 120 kg/h during (**a**) charging and (**b**) discharging of PCM packed bed. Target packed-bed temperature of 290 °C.

Enclosing the PCM in aluminum capsules created a bed structure distinct from the basalt aggregate (Figure 3). The capsules' regular geometry and increased void fraction reduced flow resistance. As a result, the pressure drop across the TES bed was significantly lower for encapsulated solar salt than for basalt aggregate at all tested air flow rates (Figure A11).

During charging, temperature profiles increased progressively from the upper section of the bed, confirming that the heating front moved from the hot-air inlet toward the lower part of the TES unit. The upper thermocouple (T top) showed similar temperature changes across all air flow rates due to its proximity to the hot-air inlet, where the local thermal response is primarily determined by the inlet air temperature and direct convective heat transfer. This pattern was also observed in the basalt-filled TES unit (Figure A4). Therefore,

the effect of air flow rate is more evident in the middle and lower sections, where heat transfer depends on the heating front's movement through the packed bed.

Higher air flow rates generally accelerated the thermal response of the PCM-packed bed, especially in the middle and lower sections of the TES unit. However, due to practical constraints, the 60 kg/h test reached a slightly higher final average packed-bed temperature (about 305 °C) compared to the 90 and 120 kg/h tests, which reached 288 °C and 294 °C, respectively. Therefore, these profiles illustrate the general impact of air flow rate on charging dynamics rather than providing a direct comparison at identical final temperatures.

During discharging, the temperature decreased more rapidly than it increased during charging, indicating more intensive heat extraction from the encapsulated PCM bed, especially at higher air flow rates. The lower thermocouple (T bot) recorded the fastest and most consistent cooling response across all air flow rates, due to its position near the cold air inlet. This area was directly exposed to the incoming cooling air, while the upper sections cooled more gradually as the cooling front moved through the TES unit.

3.2.2. Temperature Response Inside PCM Capsules

Figure 11 presents the temperature profiles measured inside the PCM capsules located in the top and middle regions of the TES column during charging and discharging. These measurements provide direct insight into the thermal response of the encapsulated solar salt, which cannot be fully identified from the external bed-temperature profiles alone.

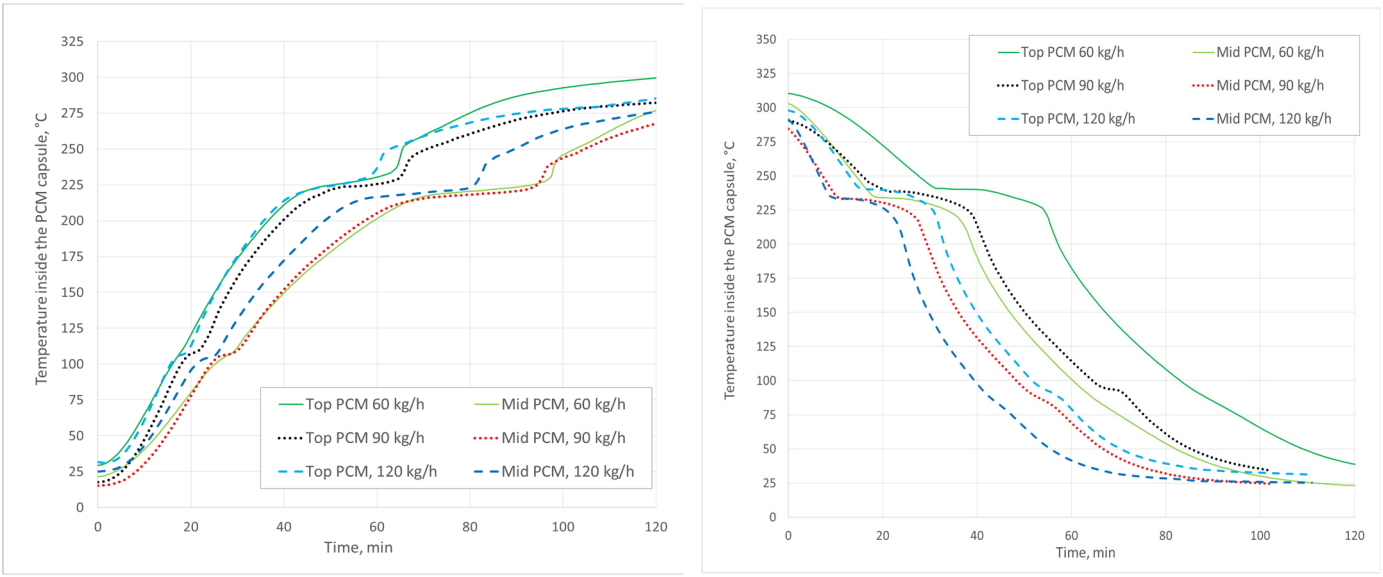


Figure 11. Temperature inside the PCM capsule during (**a**) charging and (**b**) discharging, depending on air flow rates 60–120 kg/h. Target PCM packed-bed temperature of 290 °C.

During charging, the temperature inside the PCM capsules increased more gradually than the surrounding bed temperature and displayed a clear plateau within the phase-change range. This behavior indicates that much of the supplied heat was absorbed as latent heat during melting. The plateau occurred at approximately 226–228 °C, consistent with the melting temperature determined by TG-DSC analysis.

This effect was observed in both the top and middle capsule locations, with the top PCM capsule reaching the plateau earlier due to greater exposure to incoming hot air. Increasing the air flow rate reduced the time required for the PCM to pass through the melting region, indicating more efficient heat transfer. The higher final PCM temperature

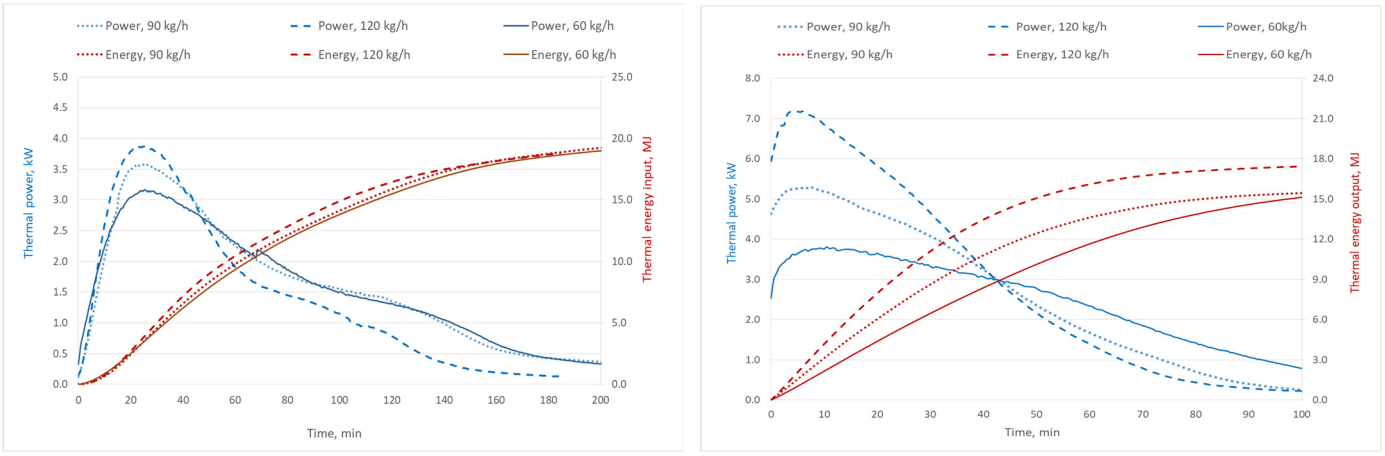
at 60 kg/h corresponds to a slightly higher final average bed temperature in this test, as previously discussed.

During discharging, the temperature inside the PCM capsules dropped rapidly at first, then exhibited a pronounced plateau as latent heat was released during solidification. This confirms that the encapsulated solar salt contributed to heat recovery through both sensible cooling and latent heat release. Higher air flow rates led to steeper temperature decreases and a shorter solidification period, indicating faster heat extraction from the PCM capsules.

While phase-change behavior is clearly visible in the internal PCM temperature profiles, it is less apparent in the overall TES column temperature profiles, as shown in Figure A12. The bed and air temperature curves remain relatively smooth during both charging and discharging, suggesting that latent heat is distributed through coupled heat transfer among the PCM, capsule walls, air flow, and neighboring capsules. Therefore, internal capsule measurements provide the most direct evidence of melting and solidification, while column temperature profiles mainly reflect the overall thermal response of the packed bed.

3.2.3. Thermal Power, Energy Storage, and Recovery

Figure 12 presents the thermal power and thermal energy input and output profiles for LHS.



(**a**) (**b**)

Figure 12. Thermal power and thermal energy input/output during (**a**) charging and (**b**) discharging, depending on air flow rates 60–120 kg/h. Target PCM packed-bed temperature of 290 °C.

Figure 12 shows that the encapsulated PCM bed exhibits a power profile similar to that of the basalt bed, but with a smoother thermal response. During charging, thermal power peaked and then gradually declined as the temperature difference between the inlet air and the PCM bed decreased. Higher air flow rates enhanced heat transfer and increased charging power, though the differences between curves were moderate. During discharging, increased air flow rates raised thermal power output and accelerated energy recovery, but also reduced the discharging period. Table 6 summarizes the detailed energy-balance parameters for the LHS configuration, and Section 3.3 provides a direct comparison with the basalt bed.

Table 6 also includes high-temperature experiments in which the packed bed was heated to approximately 400 °C. These cases are not discussed separately, as their temperature and power profiles showed similar trends to those described above. For comparison, q_{out}, q_{rec}, and ηair were evaluated up to average packed-bed temperatures of about 270 °C

for the S1–S3 tests, allowing comparison with basalt tests B4–B6, and up to 400 °C for the high-temperature series (S4–S5).

Table 6. Results of latent heat storage tests.

Process	Test	$m_{air\ avg}$, kg/h	T_{avg}, °C	P_{avg}, kW	Q_{in}/Q_{out} MJ	E_v, MJ/m^3	η_{ch}/η_d	q_{out}/q_{rec} kJ/kg$_{air}$	η_{air}	η_{TES}	Comments
Charging	S1	58	305	1.57	19.03	519	1.03	118	0.54	-	Influence of air flow rate. Target bed temperature of 280 °C.
	S2	88	288	1.58	19.35	542	0.98	139	0.39	-	
	S3	113	294	1.70	18.81	527	0.99	147	0.32	-	
	S4	46	408	2.03	24.20	627	1.07	169	0.53	-	High-temperature tests.
	S5	48	418	1.93	25.32	655	1.07	172	0.52	-	
Discharging	S1	58	289	2.08	15.88	412	0.84	125	-	83.4	Influence of air flow rate.
	S2	88	262	2.52	15.49	437	0.99	102	-	80.1	
	S3	113	263	2.64	17.58	508	0.99	77	-	93.4	
	S4	59	400	2.71	21.43	523	0.84	161	-	88.5	High-temperature tests.
	S5	120	382	3.74	23.36	626	0.99	107	-	92.3	

$m_{air\ avg}$—average flow rate and T_{avg}—average packed-bed temperature at final stage of charging or at the start of the discharging.

During charging, P_{avg} increased slightly with air flow rate in tests S1–S3, from 1.57 to 1.70 kW. Concurrently, q_{out} rose from 118 to 147 kJ/kg$_{air}$, while η_{air} decreased from 0.54 to 0.32. These results show that higher air flow rates intensified charging but reduced the fraction of thermal energy transferred to the storage bed, mainly due to shorter air residence times and earlier thermal breakthrough. A similar pattern was observed in high-temperature tests S4 and S5, where q_{out} increased to approximately 169–172 kJ/kg$_{air}$ and η_{air} remained stable at 0.52–0.53. The charging efficiency, η_{ch}, also remained close to unity for all tests, ranging from 0.98 to 1.07.

During discharging, the LHS configuration showed an expected increase in P_{avg} and a decrease in q_{rec} as the air flow rate increased. For S1–S3, P_{avg} rose from 2.08 to 2.64 kW as air flow increased from 58 to 113 kg/h, while q_{rec} fell from 125 to 77 kJ/kg$_{air}$. In S4 and S5, increasing the air flow from 59 to 120 kg/h raised P_{avg} from 2.71 to 3.74 kW and Q_{out} from 21.43 to 23.36 MJ, but reduced q_{rec} from 161 to 107 kJ/kg$_{air}$.

The recovered energy associated with LHS (not included in Table 6), accounted for 20.4–32.4% in S1–S3 and 19.3–25.1% in S4–S5 tests. In turn, the heat recovered from the packed-bed accounted for 60–70% of the total recovered heat. Discharging efficiency, η_d, was generally close to unity, though lower values were observed at the lowest air flow rates, reaching 0.84 in S1 and S4.

These results confirm a trade-off between discharging power and heat recovery per unit mass of air. Higher air flow rates intensify discharging and increase recovered power, but each kilogram of air extracts less heat from the storage bed. As expected, S4 and S5 achieved the highest E_v values, reaching 523–626 MJ/m^3, due to greater thermal energy storage at higher charging temperatures.

TES efficiency (η_{TES}) remained high for all discharging tests, ranging from 80.1% to 93.4%. This confirms that a substantial fraction of stored energy was successfully recovered during discharging. High efficiencies were also achieved in high-temperature tests, with η_{TES} reaching 88.5% and 92.3% for S4 and S5, respectively. The encapsulated solar salt bed demonstrated effective thermal energy recovery in both standard and elevated-temperature conditions.

3.3. Comparison of Sensible and Latent Heat Storage

The thermal response of SHS and LHS materials was compared using only the discharging stage. This method offers a clearer comparison, as charging is influenced by the heating column's operation and thermal inertia. Tests targeted a packed-bed temperature of approximately 290 °C.

Figure 13 shows the temperature profiles in the middle section of the TES unit during discharging for both basalt aggregate and encapsulated solar salt-packed beds. Only the middle section is shown, as it best represents the overall thermal response and is less affected by boundary conditions. The two storage materials display distinct cooling behaviors. The basalt-packed bed cools rapidly, especially at the start of discharging, reaching low temperatures quickly. In contrast, the PCM bed retains higher temperatures for longer, with less steep cooling curves over a broad temperature range.

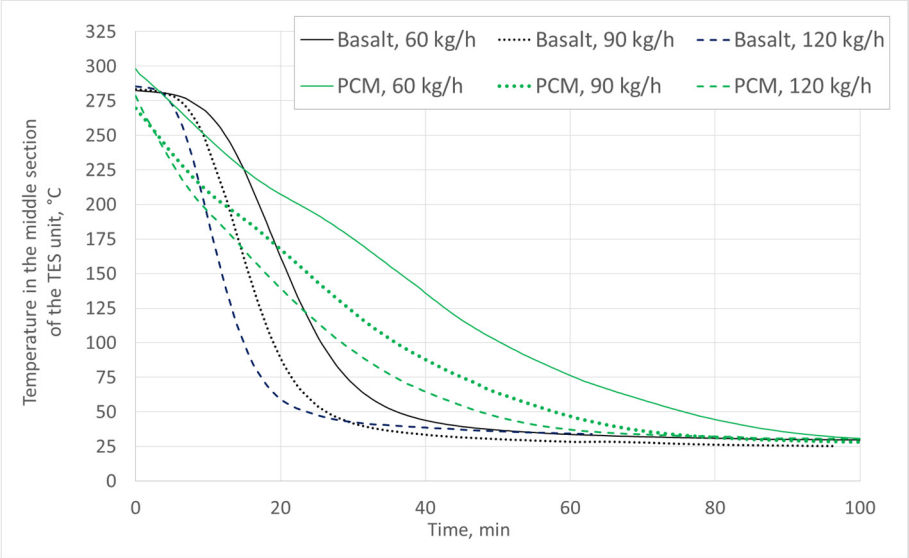


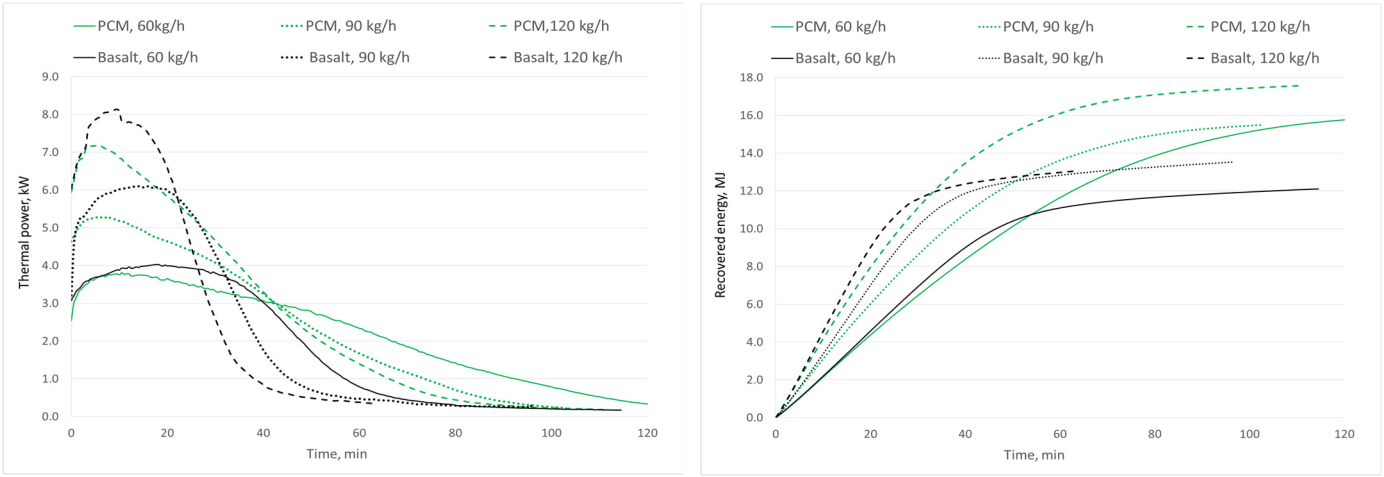
Figure 13. Comparison of temperature profiles in the middle section of the TES unit during discharging for basalt aggregate and encapsulated solar salt packed beds.

This difference becomes most apparent after the initial cooling stage. In the basalt bed, the temperature in the middle section drops sharply once the cooling front arrives. In contrast, the PCM bed shows a delayed and more gradual temperature decrease due to latent heat release during solar salt solidification and increased thermal resistance since the PCM has a low thermal conductivity. Consequently, the encapsulated PCM bed provides a longer heat-release period than the basalt bed.

This effect is observed at all tested air flow rates, though its magnitude depends on operating conditions. The 60 kg/h PCM test began at a slightly higher initial temperature, so direct quantitative comparison should be approached with caution. However, the trend is clear: the basalt bed cools more quickly, while the PCM bed maintains a longer thermal response during discharging.

For comparison, the discharging thermal power and recovered energy curves for the encapsulated PCM bed were plotted alongside those for the basalt-packed bed, as shown in Figure 14. This allows clear evaluation of the differences between sensible and latent heat storage at a target packed-bed temperature of approximately 290 °C.

The thermal power profiles differ significantly between the two packed beds. The basalt-packed bed exhibits higher, sharper power peaks, especially at higher air flow rates, followed by a rapid decline. This suggests that the sensible heat in the basalt is released quickly during the initial discharging, but the useful heat output drops off soon after. In contrast, the PCM bed exhibits broader, less abrupt power profiles. While its peak power is generally lower than that of the basalt bed, the PCM bed maintains power output for longer, particularly at low and intermediate air flow rates.



(**a**) (**b**)

Figure 14. Comparison of (**a**) thermal power output and (**b**) recovered thermal energy during discharging for basalt aggregate and encapsulated solar salt-packed beds at different air flow rates. Target packed-bed temperature: 290 °C.

The recovered energy profiles highlight further differences in discharging behavior. In the basalt bed, recovered energy rises quickly at the start and plateaus early. In the PCM bed, energy recovery increases more gradually and continues for a longer duration, resulting in higher final recovered energy at all air flow rates. These differences result from the heat storage mechanisms. The basalt bed relies solely on sensible cooling, while the PCM also releases latent heat during solidification. However, the macroencapsulated configuration introduces additional internal thermal resistance despite the high thermal conductivity of the aluminum shell. Heat must be conducted from the PCM core through the solidified PCM layer and capsule wall before being transferred to the air stream, thereby limiting the immediate heat release. This results in lower peak power and a longer discharging period. As a result, the PCM bed offers a more sustained heat-recovery profile, while the basalt bed delivers higher short-term thermal power.

It is worth mentioning that the PCM-filled TES unit contained approximately 25 kg of solar salt, and about 42 kg of basalt in SHS tests. Despite the lower mass, the PCM bed achieved higher energy recovery. This advantage is also reflected in the volumetric energy densities: the PCM bed reached 412 to 437 MJ/m^3 in tests S1–S3, compared to 293 to 345 MJ/m^3 for the basalt bed in tests B4–B6. These results confirm that solar salt PCM effectively increases the energy storage density of the TES unit.

4. Discussion

Experimental results indicate that the air flow rate primarily determines the dynamic response of the TES unit, whereas the final thermal state of the storage bed and the heat storage mechanism primarily influence the achievable energy density. In both sensible and latent heat storage systems, increasing the air flow rate speeds up charging and discharging and increases thermal power, but it does not proportionally increase the energy stored or recovered. Higher air flow rates during charging lead to greater outlet heat losses and lower air utilization efficiency, resulting in earlier thermal breakthrough and reduced gas–solid contact time. During discharging, this effect causes lower recovered energy per unit mass of air, despite higher average discharging power. Therefore, the air flow rate should be chosen to balance short-term power needs with efficient heat recovery, rather than simply maximizing it.

This observation is partly consistent with the numerical results reported by Mehrtash and Tari [26] for a macroencapsulated packed-bed LHS system. They showed that in-

creasing the HTF inlet velocity increases the average and peak charging rates, while the maximum stored energy remains nearly unchanged.

The present experiments showed a similar trend: higher air flow rates increased P_{avg} and accelerated the heating front. However, the final energy capacity depended primarily on the packed-bed temperature and the amount of storage material, rather than on the air flow rate alone. Allouhi [27] also found that increasing the air mass flow rate in an air-driven packed-bed LHS system with encapsulated adipic acid reduced storage duration, but the cumulative stored energy remained nearly unchanged.

The effect of air flow rate on PCM bed dynamics aligns with the experimental findings of Loem et al. [28], who studied RT42 paraffin in spherical capsules, using air as the heat-transfer fluid. Although their operating temperature was much lower, they also found that increasing the air mass flow rate reduced both melting and solidification times. This supports the present results, where higher air flow rates accelerated the thermal response of the encapsulated solar salt bed. Additionally, the slower temperature variation during the phase-change period matches the plateau-like behavior observed in the PCM capsules in this study.

The reduced instantaneous heat-transfer rate observed in the macro-encapsulated PCM bed results from several consecutive heat-transfer resistances. Initially, heat is transferred by convection from the air to the outer surface of the aluminum capsules. Although aluminum offers high thermal conductivity, the larger capsule size reduces the external heat-transfer area per unit PCM volume compared to irregular basalt particles. Subsequently, heat must be conducted through the capsule wall and, more importantly, through the PCM itself, which has much lower thermal conductivity than aluminum. During the phase change, the moving solid–liquid interface further increases the overall thermal resistance, since a significant fraction of the transferred heat is absorbed or released as latent heat rather than producing an immediate temperature change. Therefore, the overall charging and discharging rates are governed by the combined effects of the external convection, internal heat conduction, and the phase-change process.

Packed-bed temperature more directly affects the TES unit's storage capacity. Higher operating temperatures increase the thermal energy stored in both basalt and encapsulated solar salt beds, as well as the discharging power due to a greater temperature difference between the storage material and air. However, higher temperatures also lead to greater heat losses and larger axial temperature gradients. In the basalt bed, this increases the amount of sensible heat stored. In the PCM bed, raising the temperature above the phase-change range increases total stored energy and the proportion of sensible heat relative to latent heat. This distinction is important for PCM-based TES design, as effective latent heat utilization requires charging to a temperature sufficient for complete melting but not excessively above the phase-change temperature.

The encapsulated solar salt bed demonstrated the characteristic behavior of latent heat storage. Internal capsule measurements confirmed melting and solidification within the PCM, while the general bed temperature profiles remained smoother because the latent heat effect was distributed through the coupled heat transfer between the PCM, aluminum capsule walls, air flow, and neighboring capsules. The contribution of latent heat to recovered energy was 20.4–32.4% for the S1–S3 tests and 19.3–25.1% for the S4–S5 tests.

These results confirm that the phase-change process directly contributed to heat recovery, but the proportion of latent heat did not increase at higher charging temperatures. Wang et al. [14] reached a similar conclusion in their study of a medium–high-temperature packed-bed LHS system with encapsulated $NaNO_3/KNO_3$ mixture. In their system, latent heat contributed less than sensible heat when the bed operated above the melting range. Therefore, operation of the PCM bed should be optimized for both the final temperature and the temperature range during charging and discharging. Yang and Cai [29] support

this interpretation, showing that LHS increases total storage capacity but also extends charging time, and that the PCM melting point affects charging duration even when the final stored energy is similar.

Comparing SHS and LHS reveals distinct operational advantages. The basalt bed delivers higher short-term power output, which is useful for rapid heat extraction. In contrast, the PCM bed offers lower but more sustained thermal power, greater recovered energy, and higher volumetric energy density, even with less active storage material. The encapsulated solar salt bed achieved energy densities of 412–508 MJ/m^3 (at the packed-bed level) at near-280 °C and 523–626 MJ/m^3 in high-temperature tests. For the basalt bed at similar temperatures, values ranged from 293–345 MJ/m^3. These results align with Wang et al. [14], who reported a discharging energy of 22.20 MJ from an encapsulated nitrates PCM packed bed with a volume of about 0.042 m^3 (i.e., about 523 MJ/m^3). This confirms that the recovered energy densities in this study are consistent with previous findings for medium–high-temperature packed-bed LHS systems and highlights the potential of encapsulated solar salt to increase energy storage density in packed-bed TES units.

The geometry of the storage beds significantly affected their flow and heat-transfer characteristics. The basalt bed consisted of smaller, irregular particles, whereas the PCM bed used larger aluminum capsules arranged more uniformly. This produced a more open void structure, higher bed porosity, and more regular flow channels in the PCM bed, resulting in a significantly lower pressure drop than in the basalt bed, as shown in Figure A11. Nevertheless, overall heat-transfer performance is not determined solely by flow resistance. Larger capsules reduce the external heat-transfer area per unit PCM volume and increase the internal conduction path length, thereby limiting the instantaneous heat-transfer rate. Furthermore, the phase-change process introduces additional thermal resistance compared with sensible heat storage. Capsule geometry is therefore a critical design parameter. Mol et al. [30] found that smaller PCM particles improved heat transfer with the HTF, leading to faster charging and discharging. Klitou et al. [31] and Allouhi [27] also showed that bed porosity, PCM mass, and HTF flow rate together influence charging dynamics and storage capacity. These results indicate that optimizing capsule size, packing density, and bed porosity is necessary to balance heat transfer rate, pressure drop, PCM mass, and volumetric energy density.

The comparison between the basalt and PCM beds focused mainly on the discharging stage, which better reflects heat recovery performance. Differences in final charging temperatures, especially for the 60 kg/h PCM test, along with residual heat and unavoidable thermal losses during the transition between charging and discharging, should be considered when evaluating recovered energy and TES recovery efficiency.

Compared with previous experimental studies, the present work provides one of the few direct comparisons between sensible and latent heat storage performed in the same packed-bed scale using identical operating conditions. Unlike many studies that focus primarily on numerical modeling or single-capsule characterization, this investigation evaluates the behavior of approximately 25 kg of macroencapsulated commercial solar salt in a 25 dm^3 packed bed. This allows the thermal response, energy density, and efficiency of SHS and LHS systems to be compared under conditions that are practically relevant.

Future research should prioritize optimizing the encapsulation geometry and operating temperature range of the PCM bed. Specifically, studies should examine the effects of capsule size, wall thickness, packing arrangement, and PCM mass fraction on the balance among latent heat utilization, heat transfer rate, pressure drop, and volumetric energy density. Additional work should address repeated charging and discharging cycles, long-term material compatibility, and numerical modeling of coupled sensible–latent heat transfer in encapsulated PCM-packed beds.

5. Conclusions

This study experimentally compared sensible and latent heat storage in an air-based packed-bed TES unit using basalt aggregate and encapsulated solar salt (60 wt.% $NaNO_3$–40 wt.% KNO_3) as storage materials. The effects of air flow rate and operating temperature on the thermal performance of both storage concepts were evaluated. The main conclusions are as follows:

1. Air flow rate mainly influenced charging and discharging dynamics. Increasing the air flow rate from about 60 to 120 kg/h increased the average charging power from 0.85–1.31 kW to 0.94–1.64 kW and the average discharging power from 1.25–2.39 kW to 1.64–3.98 kW for the basalt bed. The PCM bed showed a similar increase, with charging power rising to 1.57–1.70 kW and discharging power to 2.08–3.74 kW. However, the total stored and recovered thermal energy in each configuration depended primarily on the final packed-bed temperature and varied only slightly with the air flow rate.
2. Higher air flow rates reduced the effective utilization of the thermal energy supplied by the air stream. During charging, the air utilization efficiency decreased from 0.79–0.58 to 0.31–0.22 for the basalt bed and from 0.54 to 0.32 for the PCM bed, indicating earlier thermal breakthrough, consistent with the shorter residence time of the air in the packed bed. During discharging, higher air flow rates increased thermal power but reduced the specific recovered thermal energy (q_{rec}) per unit mass of air, for example from 74 to 17 kJ/kg_{air} for the basalt bed and from 125 to 77 kJ/kg_{air} for the PCM bed.
3. The final thermal state of the packed bed primarily determines energy density. For the basalt bed, volumetric energy density (calculated from recovered energy) increased from 108–160 MJ/m^3 at approximately 150 °C to 351–405 MJ/m^3 above 320 °C. For the PCM bed, recovered energy densities reached 412–508 MJ/m^3 near 290 °C and 523–626 MJ/m^3 in high-temperature tests.
4. The encapsulated solar salt showed clear LHS behavior and significantly increased the energy storage capacity of the TES unit. Internal capsule measurements confirmed melting and solidification at 226–228 °C, while latent heat contributed 19–32% of the recovered thermal energy. At comparable operating temperatures, the PCM bed achieved recovered volumetric energy densities of 412–437 MJ/m^3, compared with 292–345 MJ/m^3 for the basalt bed, corresponding to an increase of approximately 20–50%.
5. Both storage concepts demonstrated high TES efficiency, ranging from 80.5% to 93.7% for the basalt bed and from 80.1% to 93.4% for the PCM bed, confirming effective thermal energy recovery over the investigated operating range.
6. The two storage concepts provide complementary operational benefits. The basalt bed offers higher short-term thermal power and faster heat release, while the encapsulated PCM bed enables longer discharge duration, higher recovered energy, and significantly greater volumetric energy density. These findings indicate that encapsulated solar salt is a promising storage medium for medium- and high-temperature packed-bed TES systems requiring high energy density and extended heat delivery.

Future research should optimize capsule geometry, PCM loading, and operating temperature, as well as address long-term cyclic stability and validating numerical models of coupled sensible and latent heat transfer.

Supplementary Materials: The following supporting information can be downloaded at: https://www.mdpi.com/article/10.3390/en19133196/s1, Figure S1. Repeatability test for charging experiment S5. Comparison of the original (solid line) and repeated experiment (dashed line). Figure S2. The inlet air temperature and the average packed-bed temperature for tests B1 and B3.

Author Contributions: Conceptualization, T.S.; methodology, T.S. and S.D.; validation, T.S. and S.D.; formal analysis, T.S.; investigation, T.S. and S.D.; resources, S.D. and A.C.; data curation, T.S.;

writing—original draft preparation, T.S. and K.K.; writing—review and editing, T.S., K.K. and R.F.; visualization, T.S.; supervision, A.C.; project administration, A.C.; funding acquisition, A.C. All authors have read and agreed to the published version of the manuscript.

Funding: The work presented in this paper was performed as part of the HESS project (Hybrid energy storage system using postmining infrastructure) grant no. 101112380 supported by the European Research Fund for Coal and Steel (EU RFCS).

Data Availability Statement: The original contributions presented in this study are included in the article and Appendix A. The raw data supporting the conclusions of this article will be made available by the authors on request.

Acknowledgments: We would like to kindly thank Tomasz R. from ITPE for his technical support with the DSC/TGA analysis of the solar salt sample, and Jakub O. from the Silesian University of Technology for providing the basalt sample. During the preparation of this manuscript, the authors used ChatGPT 5.5 and Grammarly Pro (v.1.165.1.0) to improve the clarity of the text and organize the structure of the paper (text editing, removing repetitions). In addition, ChatGPT 5.5 was used to create a graphical abstract. The authors have reviewed and edited the output and take full responsibility for the content of this publication.

Conflicts of Interest: The authors declare no conflicts of interest. The funders had no role in the design of the study; in the collection, analyses, or interpretation of data; in the writing of the manuscript; or in the decision to publish the results.

Abbreviations

The following abbreviations are used in this manuscript:

HTF	Heat transfer fluid
LHS	Latent heat storage
PBTES	Packed-bed thermal energy storage
PCM	Phase change material
SHS	Sensible heat storage
TES	Thermal energy storage

Appendix A

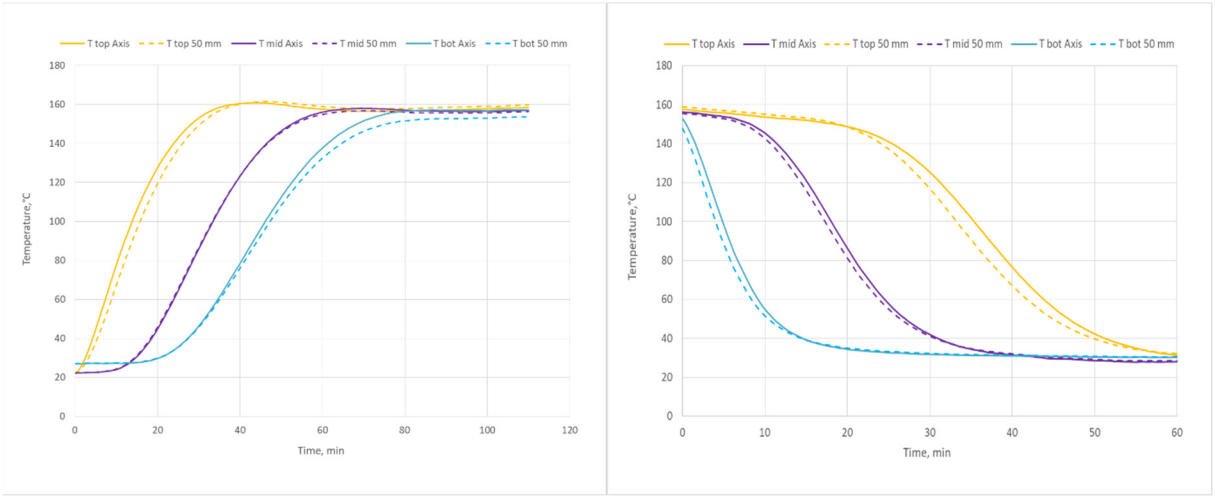
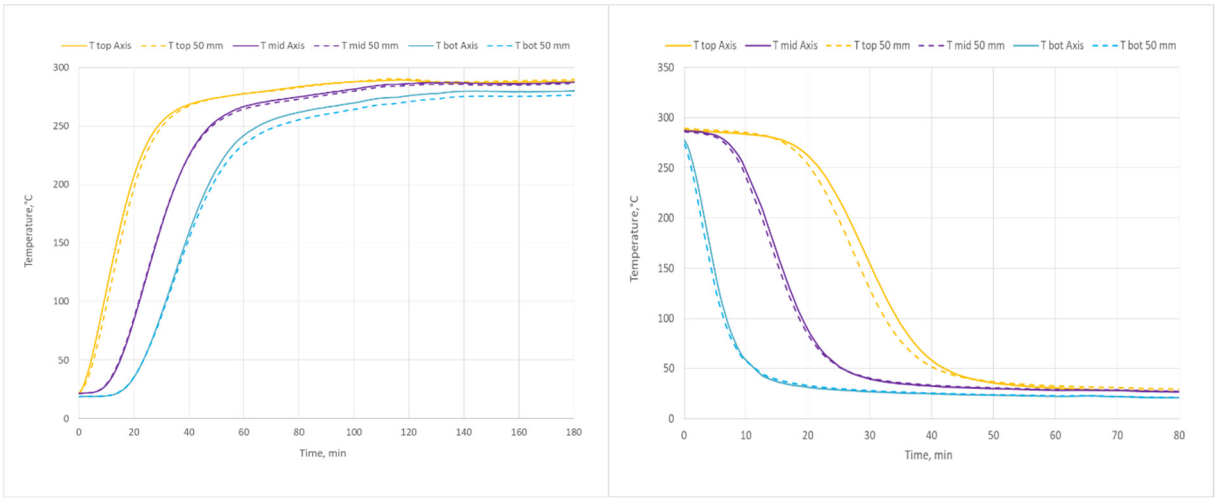
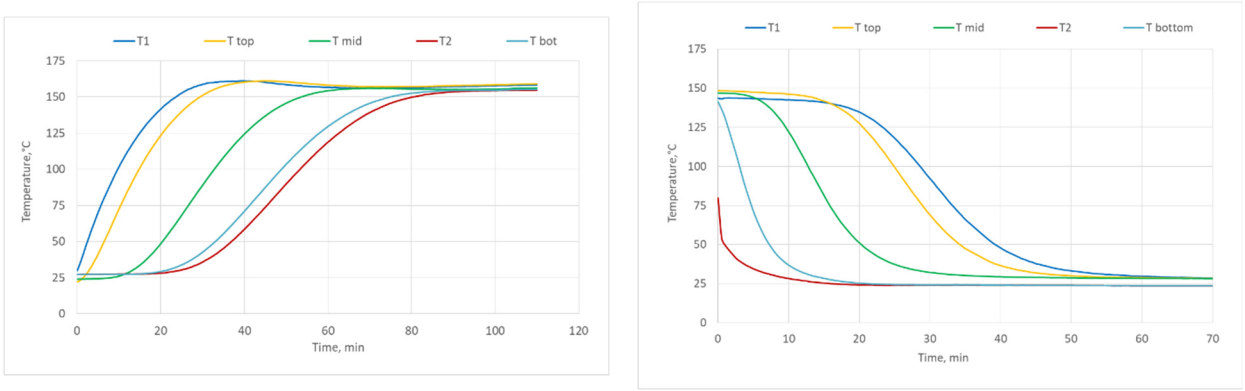


Figure A1. Temperature profiles in the TES unit along the column axis and 50 mm from the axis during (**a**) charging and (**b**) discharging. Air flow rate of 60 kg/h and target basalt packed-bed temperature of 150 °C (test B1).



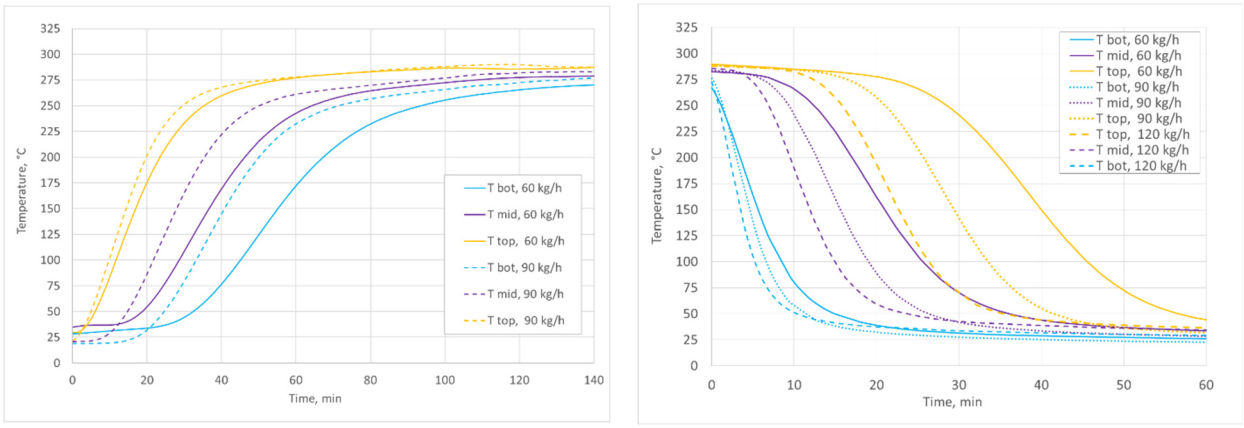
(**a**) (**b**)

Figure A2. Temperature profiles in the TES unit along the column axis and 50 mm from the axis during (**a**) charging and (**b**) discharging. Air flow rate of 90 kg/h and target basalt packed-bed temperature of 290 °C (test B5).



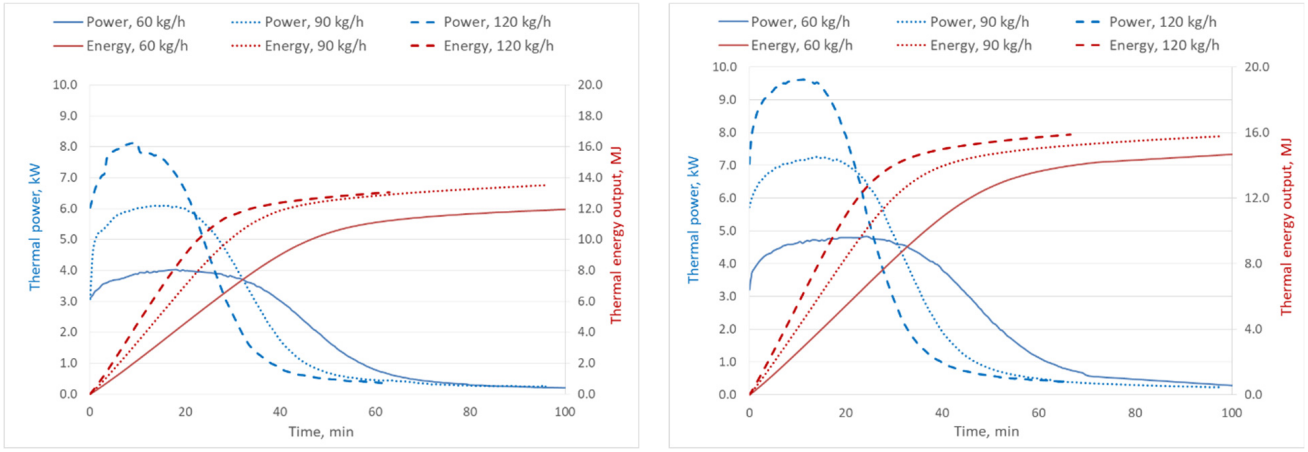
(**a**) (**b**)

Figure A3. Temperature distribution in the basalt packed bed during (**a**) charging and (**b**) discharging. Target basalt packed-bed temperature of 150 °C and air flow rate of 90 kg/h (test B2).



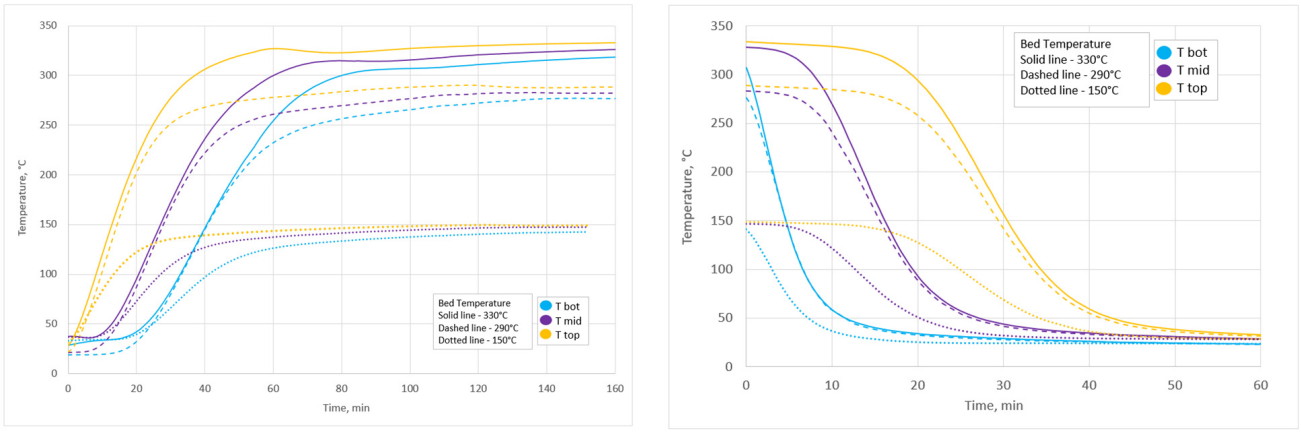
(**a**) (**b**)

Figure A4. Temperature distribution during (**a**) charging and (**b**) discharging of the TES unit at various air flow rates. Target basalt packed-bed temperature of 290 °C (tests B4–B6).



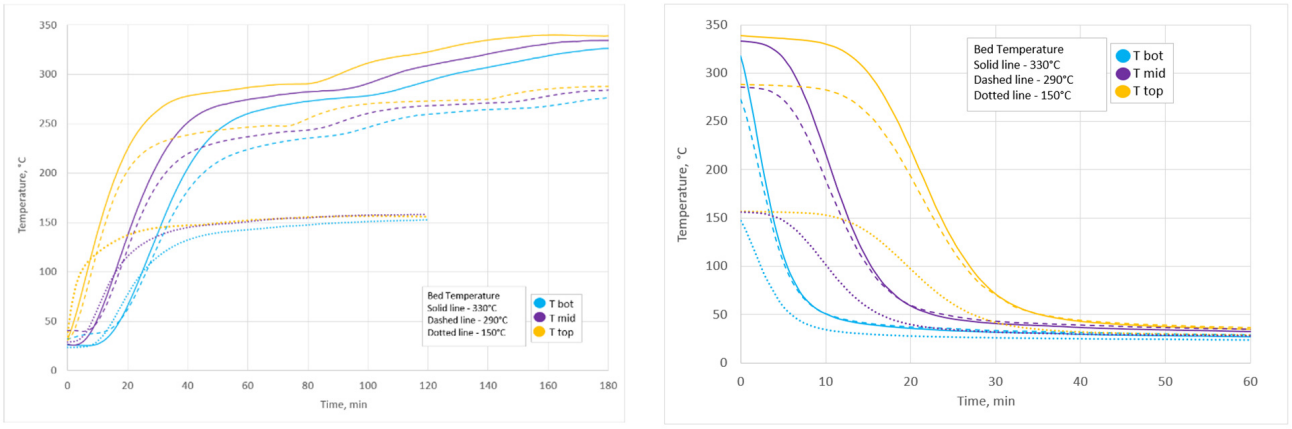
(**a**) (**b**)

Figure A5. Thermal power and recovered energy at various air flow rates during discharging basalt packed bed at target temperatures of (**a**) 290 °C and (**b**) 330 °C (tests B4–B9).



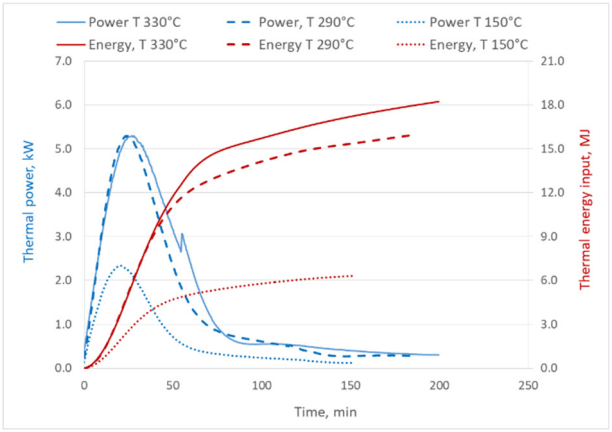
(**a**) (**b**)

Figure A6. Temperature profiles of the TES unit depending on basalt packed-bed temperature; (**a**) charging and (**b**) discharging. Air flow rate of 90 kg/h (tests B2, B5, B8).

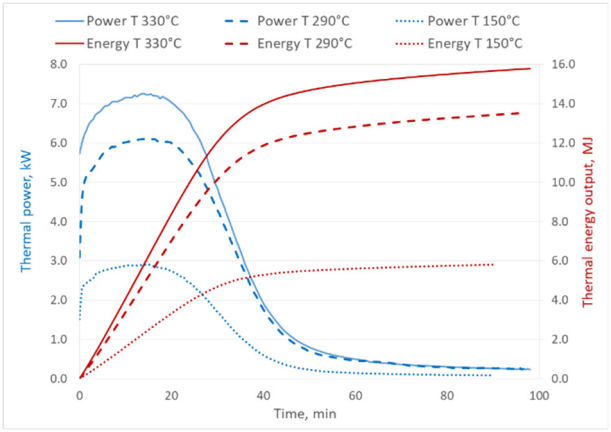


(**a**) (**b**)

Figure A7. Temperature profiles of the TES unit depending on basalt packed-bed temperature; (**a**) charging and (**b**) discharging. Air flow rate of 120 kg/h (tests B3, B6, B9).

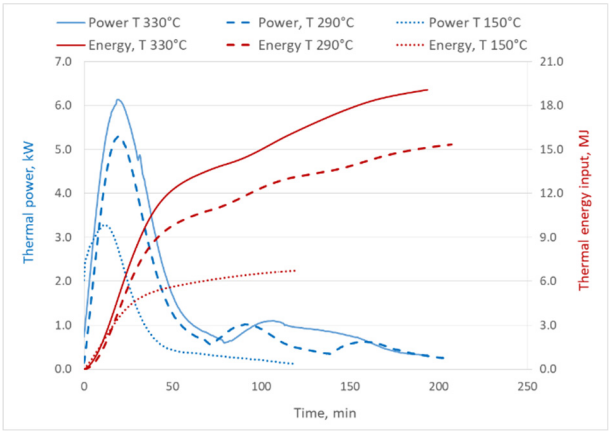


(**a**)

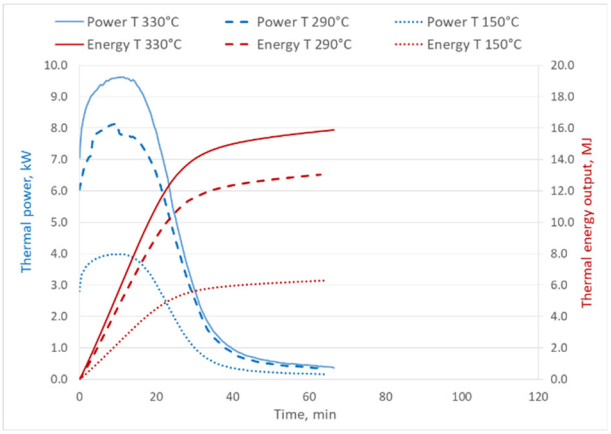


(**b**)

Figure A8. Thermal power and thermal energy of the TES unit depending on basalt packed-bed temperature; (**a**) charging and (**b**) discharging. Air flow rate of 90 kg/h (tests B2, B5, B8).



(**a**)



(**b**)

Figure A9. Thermal power and thermal energy of the TES unit depending on basalt packed-bed temperature; (**a**) charging and (**b**) discharging. Air flow rate of 120 kg/h (tests B3, B6, B9).

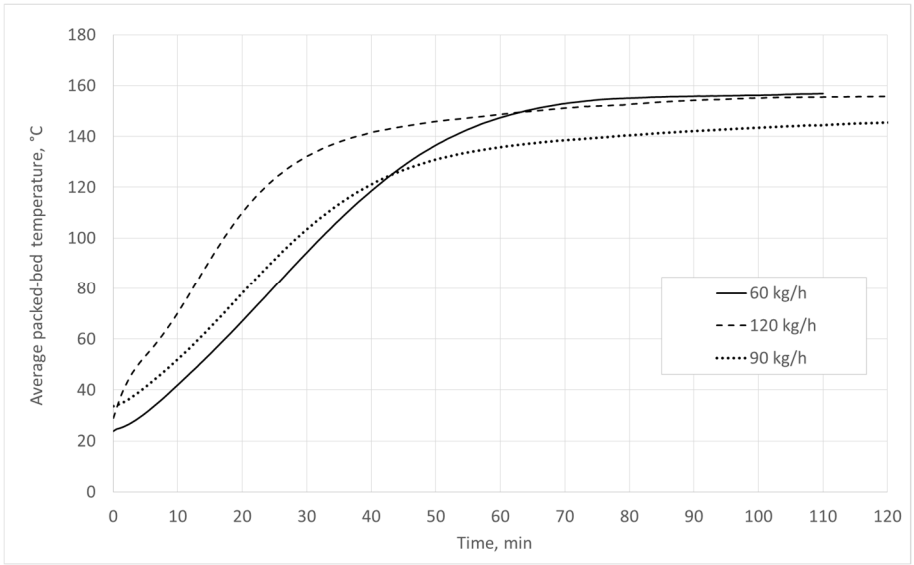


Figure A10. Average basalt packed-bed temperatures for tests B1–B3.

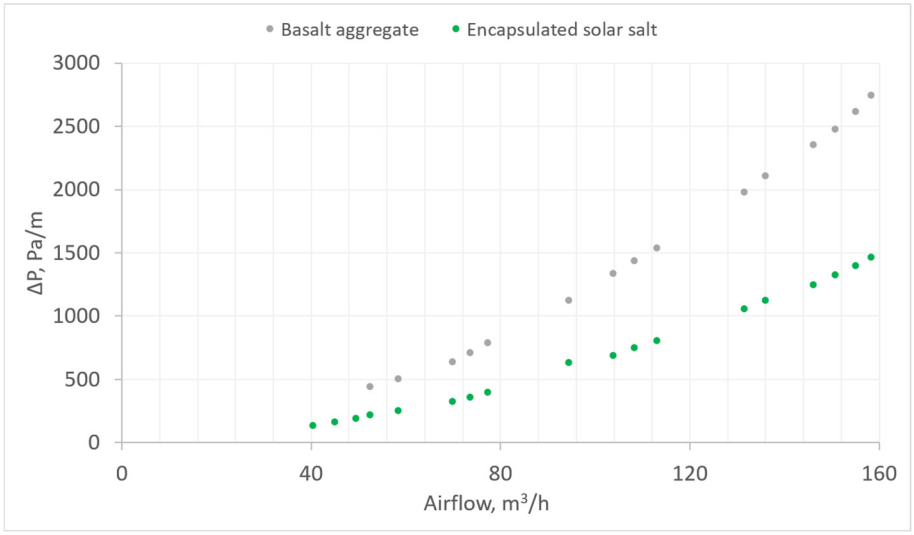
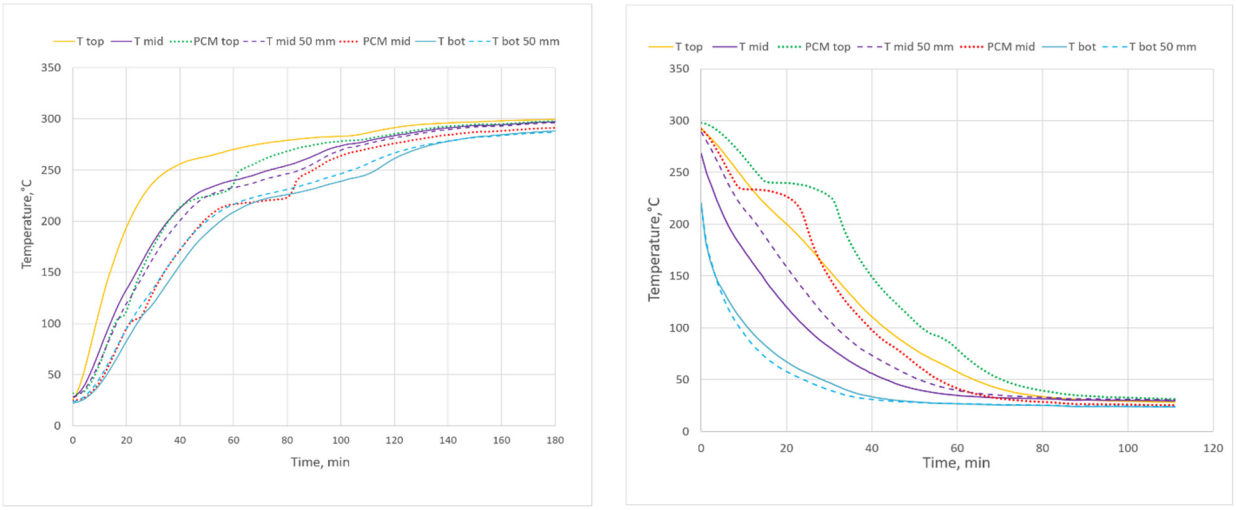


Figure A11. Measured pressure drop in the TES unit.



(**a**) (**b**)

Figure A12. Temperature profiles of the PCM packed bed during (**a**) charging and (**b**) discharging. Temperatures measured away from the column axis and inside the PCM capsules are also included (test S3).

References

1. Koohi-Fayegh, S.; Rosen, M.A. A Review of Energy Storage Types, Applications and Recent Developments. *J. Energy Storage* **2020**, *27*, 101047. [CrossRef]
2. Vallese, L.; Javadi, H.; Badenes, B.; Urchueguia, J.F.; Lombardo, G.; Menegazzo, D.; Ure, Z.; Cesari, S.; Bottarelli, M.; Baccega, E.; et al. A Comprehensive Review of Thermal Energy Storage Technologies and Their Applications: Creation of a Database. *Renew. Sustain. Energy Rev.* **2026**, *225*, 116133. [CrossRef]
3. Spietz, T.; Fryza, R.; Lasek, J.; Zuwała, J. Thermochemical Energy Storage Based on Salt Hydrates: A Comprehensive Review. *Energies* **2025**, *18*, 2643. [CrossRef]
4. Das, D.; Crosby, R.; Paul, M.C. A Comprehensive Review on the Form Stable Phase Change Materials for Storing Renewable Heat Preparation, Characterization and Application. *J. Energy Storage* **2025**, *110*, 115284. [CrossRef]
5. Yang, Z.L.; Walvekar, R.; Wong, W.P.; Sharma, R.K.; Dharaskar, S.; Khalid, M. Advances in Phase Change Materials, Heat Transfer Enhancement Techniques, and Their Applications in Thermal Energy Storage: A Comprehensive Review. *J. Energy Storage* **2024**, *87*, 111329. [CrossRef]
6. Jurczyk, M.; Spietz, T.; Czardybon, A.; Dobras, S.; Ignasiak, K.; Bartela, Ł.; Uchman, W.; Ochmann, J. Review of Thermal Energy Storage Materials for Application in Large-Scale Integrated Energy Systems—Methodology for Matching Heat Storage Solutions for Given Applications. *Energies* **2024**, *17*, 3544. [CrossRef]

7. Georgousis, N.; Diriken, J.; Speetjens, M.; Rindt, C. Comprehensive Review on Packed-Bed Sensible Heat Storage Systems. *J. Energy Storage* **2025**, *121*, 116516. [CrossRef]
8. Sun, B.; Liu, Z.; Ji, X.; Gao, L.; Che, D. Thermal Energy Storage Characteristics of Packed Bed Encapsulating Spherical Capsules with Composite Phase Change Materials. *Appl. Therm. Eng.* **2022**, *201*, 117659. [CrossRef]
9. Pourhemmati, S.; Hossainpour, S.; Haeri, S.Z. Experimental and Numerical Investigation of Packed-Bed Thermal Energy Storage Utilizing Two Phase Change Materials (PCM) in Spherical Capsules. *Int. J. Therm. Sci.* **2025**, *210*, 109605. [CrossRef]
10. Pielichowska, K.; Pielichowski, K. Phase Change Materials for Thermal Energy Storage. *Prog. Mater. Sci.* **2014**, *65*, 67–123. [CrossRef]
11. Cui, J.; Yang, X.; Xu, H.; Zhuang, Z.; Xie, J. Multi-Scale Investigations of Packed Bed Latent Thermal Energy Storage Systems: Perspectives from Material Selection to Applications. *Int. J. Heat Mass Transf.* **2026**, *255*, 127773. [CrossRef]
12. Costa, S.-C.; Mahkamov, K.; Kenisarin, M.; Ismail, M.; Lynn, K.; Halimic, E.; Mullen, D. Solar Salt Latent Heat Thermal Storage for a Small Solar Organic Rankine Cycle Plant. *J. Energy Resour. Technol.* **2019**, *142*, 031203. [CrossRef]
13. Han, Z.; Wickramaratne, C.; Yogi Goswami, D.; Jotshi, C. Experimental Study on Operating Characteristics of Nitrate Salt-Based Latent Heat Thermal Energy Storage Unit. *Appl. Therm. Eng.* **2022**, *202*, 117846. [CrossRef]
14. Wang, W.; He, X.; Shuai, Y.; Qiu, J.; Hou, Y.; Pan, Q. Experimental Study on Thermal Performance of a Novel Medium-High Temperature Packed-Bed Latent Heat Storage System Containing Binary Nitrate. *Appl. Energy* **2022**, *309*, 118433. [CrossRef]
15. Laing, D.; Bauer, T.; Breidenbach, N.; Hachmann, B.; Johnson, M. Development of High Temperature Phase-Change-Material Storages. *Appl. Energy* **2013**, *109*, 497–504. [CrossRef]
16. Johnson, M.; Fiss, M. Superheated Steam Production from a Large-Scale Latent Heat Storage System within a Cogeneration Plant. *Commun. Eng.* **2023**, *2*, 68. [CrossRef]
17. Li, M.-J.; Li, M.-J.; Fan, C.-H.; Liu, Z.-B. Experimental Study on the Thermal Performance of a Large 100 MJ Cascaded Packed-Bed Thermal Energy Storage System with Macro-Encapsulation of Phase Change Materials. *J. Energy Storage* **2025**, *128*, 117193. [CrossRef]
18. Jia, G.; Yuan, X.; Cao, Y.; Jiang, K.; Yang, Y.; Chen, Z.; Cheng, G.; Zou, Y. Experimental and Numerical Investigation into a Thermocline Storage for District Heating. *Appl. Therm. Eng.* **2024**, *245*, 122748. [CrossRef]
19. Touzo, A.; Olives, R.; Dejean, G.; Pham Minh, D.; El Hafi, M.; Hoffmann, J.-F.; Py, X. Experimental and Numerical Analysis of a Packed-Bed Thermal Energy Storage System Designed to Recover High Temperature Waste Heat: An Industrial Scale Up. *J. Energy Storage* **2020**, *32*, 101894. [CrossRef]
20. Ochmann, J.; Jurczyk, M.; Bartela, Ł. Role of Thermal Energy Storage Technology in the Decarbonization of Energy Sector Process—Packed Rock Bed Parameters Analysis. *Archit. Civ. Eng. Environ.* **2023**, *15*, 65–74. [CrossRef]
21. Waples, D.W.; Waples, J.S. A Review and Evaluation of Specific Heat Capacities of Rocks, Minerals, and Subsurface Fluids. Part 1: Minerals and Nonporous Rocks. *Nat. Resour. Res.* **2004**, *13*, 97–122. [CrossRef]
22. Hartlieb, P.; Toifl, M.; Kuchar, F.; Meisels, R.; Antretter, T. Thermo-Physical Properties of Selected Hard Rocks and Their Relation to Microwave-Assisted Comminution. *Miner. Eng.* **2016**, *91*, 34–41. [CrossRef]
23. Kenisarin, M.M. High-Temperature Phase Change Materials for Thermal Energy Storage. *Renew. Sustain. Energy Rev.* **2010**, *14*, 955–970. [CrossRef]
24. Vignarooban, K.; Xu, X.; Wang, K.; Molina, E.E.; Li, P.; Gervasio, D.; Kannan, A.M. Vapor Pressure and Corrosivity of Ternary Metal-Chloride Molten-Salt Based Heat Transfer Fluids for Use in Concentrating Solar Power Systems. *Appl. Energy* **2015**, *159*, 206–213. [CrossRef]
25. Zavoico, A.B. *Solar Power Tower—Design Basis Document*; Sandia National Labs: Albuquerque, NM, USA, 2001. [CrossRef]
26. Mehrtash, M.; Tari, I. Parametric Sensitivity Analysis and Performance Evaluation of High-Temperature Macro-Encapsulated Packed-Bed Latent Heat Storage System Operating with Transient Inlet Boundary Conditions. *Processes* **2022**, *10*, 1382. [CrossRef]
27. Allouhi, A. Latent Thermal Energy Storage for Solar Industrial Drying Applications. *Sustainability* **2023**, *15*, 13254. [CrossRef]
28. Loem, S.; Deethayat, T.; Asanakham, A.; Kiatsiriroat, T. Thermal Characteristics on Melting/Solidification of Low Temperature PCM Balls Packed Bed with Air Charging/Discharging. *Case Stud. Therm. Eng.* **2019**, *14*, 100431. [CrossRef]
29. Yang, X.; Cai, Z. An Analysis of a Packed Bed Thermal Energy Storage System Using Sensible Heat and Phase Change Materials. *Int. J. Heat Mass Transf.* **2019**, *144*, 118651. [CrossRef]
30. Mol, J.; Shahi, M.; Mahmoudi, A. Numerical Modeling of Thermal Storage Performance of Encapsulated PCM Particles in an Unstructured Packed Bed. *Energies* **2020**, *13*, 6413. [CrossRef]
31. Klitou, A.; Klitou, T.; Fokaides, P.A. Modelling a Packed-Bed Latent Heat Thermal Energy Storage Unit and Studying Its Performance Using Different Paraffins. *Int. J. Sustain. Energy* **2024**, *43*, 2306416. [CrossRef]

Disclaimer/Publisher's Note: The statements, opinions and data contained in all publications are solely those of the individual author(s) and contributor(s) and not of MDPI and/or the editor(s). MDPI and/or the editor(s) disclaim responsibility for any injury to people or property resulting from any ideas, methods, instructions or products referred to in the content.